Design and Analysis of LCD-Based Modulator for Passive Sunlight Communications

Sahar Ammar, Osama Amin, Mohamed-Slim Alouini, and Basem Shihada

***Abstract*—Solar energy is widely used for electricity generation, heating systems, and indoor environment daytime illumination. Indeed, large amounts of sunlight energy remain insufficiently used. In this work, we aim at employing sunlight energy for data transmission as a green option for wireless communications. Being emitted by an uncontrollable source, taming the sunlight is a challenging task that requires appropriate technologies to manipulate incident light. Liquid crystal devices are switchable glass technologies that have adequate response time and contrast characteristics for such an application. In this regard, we design a novel dual-cell liquid crystal shutter (DLS) by stacking two liquid crystal cells that operate in opposite manners, and we build our sunlight modulator with an array of DLSs. Then, we adopt time division multiplexing and polarization-based modulation to boost the data rate and eliminate the flickering effect. In addition, we provide mathematical modeling of the system and study its performance in terms of communication and energy consumption. Finally, we introduce some numerical results to examine the impact of multiple parameters on the system's performance and compare it with the state-of-the-art, which showed that our system features higher data rates and extended link ranges.**

***Index Terms*—Sunlight communication, liquid crystal devices (LCDs), liquid crystal shutter, solar irradiance, time division multiplexing, polarization modulation.**

I. Introduction

WIRELESS communication technologies are typically based on either radio frequency (RF) communication, which mainly suffers from a congested frequency band, or optical communication, which requires energy expensive active light sources, such as lasers and light-emitting diodes (LEDs) [1]. Whereas, considerable amounts of ambient light remain unexploited and are mainly used for illumination purposes. Such light can be modulated to transmit data offering a complementary solution for wireless communications [2]. As such, this way would not only provide an unlicensed wide optical band including visible and infrared ranges, but it would also help to save energy by reducing the usage of other light sources, particularly during the day when sunlight can be exploited instead. Such communication would avoid the interference between the signal of a visible light communication (VLC) link and the background light, i.e., the sunlight. It could be used for Internet of things (IoT) applications, especially in indoor environments, which require low data rates and low energy consumption. However, this light is emitted by uncontrollable sources, such as the sun or light bulbs, making it difficult to manipulate. Switchable glass technologies that can be embedded in surfaces, e.g., windows, to modulate the incoming light, can be a solution to such a problem.

Switchable glass, or smart glass is a technology that allows controlling light transmission by an applied voltage [3], [4]. It has two states; a clear state when light transmission is allowed and a dark state when the light is blocked. The time necessary for the transition between these states is referred to as the switching time, or the speed of the smart glass, and it is considered a critical technology feature due to its direct impact on the achievable data rate [5]. Another characteristic is the contrast reflecting the difference in the light intensity transmitted during each state, which can affect the system's bit error ate (BER) and link range. There are two main light controlling categories known as MEMS-based micro-shutters and Electrolyte-based devices, which includes electrochromic devices (ECDs), suspended particle devices (SPDs) and liquid crystal devices (LCDs). Smart glass is usually utilized for daylight shading and steering by absorbing or scattering the light to control its transmission or deflect it in certain directions to illuminate specific areas [6]. Nevertheless, it is not commonly used for wireless communication purposes mainly due to its long switching times. In particular, ECDs and SPDs are not suitable for such application as their performances need to be further optimized in terms of speed and contrast [3], [7], [8]. On the other hand, MEMS-based micro-shutters provide short switching times and high contrast, but they can be energy inefficient and they are still in research stage [6], [9], [10]. Meanwhile, LCDs offer high contrast and rapid speed making it adequate for the target applications [11]. Also, their low energy consumption and commercial availability encouraged researchers to design passive communication systems based on LCDs.

Several works have been reported in the literature developing practical systems utilizing LCDs for light modulation to establish Backscatter communications [12], [13], [14], [15], [16] or Sunlight communications [5], [17], [18]. Backscatter communication based on retro-reflective fabric was mainly demonstrated in [12], [13], [14]. RetroTurbo is the current pioneer practical system that built a backscatter VLC system using an array of 64 LCDs [12]. It achieves the highest data rate in the literature with 8 $Kbps$ over 7.5 m by using the delayed superimposition modulation and polarization-based quadrature amplitude modulation

Manuscript received 15 August 2022; accepted 17 August 2022. Date of publication 22 August 2022; date of current version 2 September 2022. The work was supported by the King Abdullah University of Science and Technology. *(Corresponding author: Basem Shihada.)*

The authors are with the CEMSE Division, King Abdullah University of Science and Technology, Thuwal 23955, Saudi Arabia (e-mail: sahar.ammar@kaust.edu.sa; osama.amin@kaust.edu.sa; slim.alouini@kaust.edu.sa; basem.shihada@kaust.edu.sa).

Digital Object Identifier 10.1109/JPHOT.2022.3200833

(PQAM) to exploit the entire channel time and polarization dimensions. RetroTurbo uses an equalizer with a channel training algorithm to mitigate the introduced inter-symbol interference (ISI). Moreover, the most recent work exploiting sunlight light, is ChromaLux where the authors reveal a transient state of LCDs by stacking 4 to 6 cells forming a single pixel transmitter and showing shorter switching times [17]. Using this transient state, they propose a three-level polarization based modulation technique allowing them to reach long communication ranges (up to 50 m) and a data rate of 1 $Kbps$. Another interesting system was introduced in [5] featuring a long link range up to 65 m with 80 bps as data rate. The system is composed of a single LCD and an energy efficient photo-transistor working with a novel frequency-based modulation method to achieve flicker-free Sunlight communication. Moreover, PIXEL builds a visible light positioning system based on a light to camera VLC link [18]. The communication system adopts polarization-based modulation and color shift keying to modulate ambient light and achieve a data rate of 14 bps over 10 m.

In this paper, we design a novel dual-cell liquid crystal shutter (DLS) and utilize it to develop and study a passive optical communication system that modulates the Sunlight by profiting from the properties of LCDs. We also provide a comprehensive theoretical analysis of LCDs in general and DLSs in particular, which complements the recent experimental implementations of passive communication systems. The contributions of our work are as follows:

- Designing a novel DLS system by stacking two liquid crystal (LC) cells operating in opposite manners. The design offers fast and symmetrical switching times and addresses the issues of the flicker effect and the inter-symbol interference.
- Developing an improved design of sunlight modulator that efficiently utilizes the time and polarization dimensions to boost the data rate.
- Providing a mathematical modeling of the proposed system including the modulator and the sunlight modulation channel.
- Analyzing the energy requirements of the system based on practical systems.

The rest of this paper is organized as follows, Section II provides the fundamentals of LCDs. Section III describes the proposed sunlight communication system with the DLS design. Section IV presents the mathematical modeling of the system. Section V deals with the performance analysis and Section VI discusses the numerical results. Finally, Section VII provides the energy consumption analysis followed by the paper conclusion in Section VIII.

II. Background on Liquid Crystal Devices

A. Fundamentals of Liquid Crystals

LCs are states of matter having intermediate properties between liquid and solid states [19]. They have multiple classifications based mainly on the properties of the material itself. We are interested in the Nematic LCs which are the class of LCs used in the development of LC optical shutters technologies.

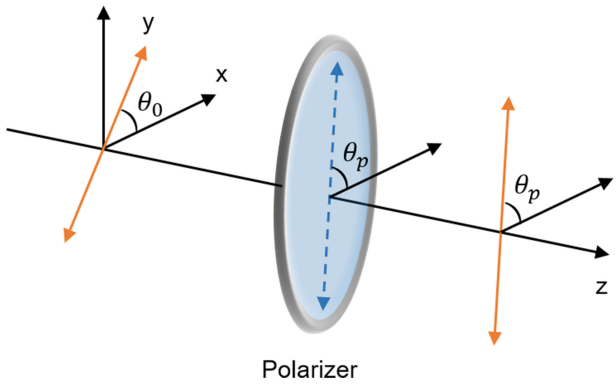

Fig. 1. Illustration of the polarizer effect on the polarized light [20].

The structure and mechanism of LCDs are based on fundamental concepts of physics and optics including mainly the polarization of light waves and the birefringence of the LC material.

- *Polarization:* is a basic property of electromagnetic waves including optical waves which are composed of orthogonal vibrating electric and magnetic fields [20]. The light polarization defines the direction of the oscillations of the electric field. An optical wave is referred to as polarized light if it is oscillating in one plane while considered unpolarized if the oscillations occur in more than one plane. A polarized light with certain polarization can be generated when light propagates through a polarizer as shown in Fig. 1 where the polarizer, with polarization axis having an angle θ_{p} with axis x, acts as an optical filter allowing the passage of only the light component with the same polarization direction. The intensity of the emerging light (considering an ideal polarizer), I_{p}, is modeled by *Malus's law* as [20],

$$I_p = I_0 \cos^2(\theta_p - \theta_0) \tag{1}$$

  where I_0 and θ_0 are the intensity and the angle of the polarization direction of the incoming light. If the incident light is unpolarized, then the intensity of the output beam is $I_{\mathrm{p}} = I_0/2$. Also, if the light has a polarization perpendicular to the polarizer axis ($\theta_{\mathrm{p}} - \theta_0 = 0$), the polarizer should ideally block light passage totally ($I_{\mathrm{p}} = 0$), however, practical polarizers would still permit the transmission of a fraction of light.
- *Birefringence:* is an optical property of materials with refractive index depending on the direction of incident light (both propagation and polarization directions) [19]. Such property induces a double refraction of the incoming light where the beam is split into two rays namely the ordinary ray and the extraordinary ray. These rays take two different directions while propagating through the material, and have two different indices n_{o} and n_{e}, for the ordinary ray and the extraordinary ray, respectively. The birefringence is defined as the difference between these indices, which is given by $\Delta n = n_{\mathrm{e}} - n_{\mathrm{o}}$, [19].

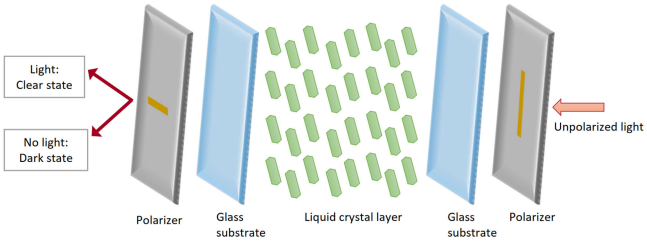

Fig. 2. General structure of nematic LCDs with a NW configuration.

B. Nematic Liquid Crystal Devices

In general, a nematic LCD is composed of a LC layer sandwiched between two glass substrates and equipped with two polarizers as illustrated in Fig. 2. Such structure forms a single-cell LCD while a dual-cell LCD includes two stacked LC layers with four glass substrates. Also, two LCD configurations can be distinguished based on the angle between the polarizers axis [19]. A nematic LCD is operating in a normally white (NW) configuration, if its polarizers are perpendicular and it has a normally black (NB) configuration when the polarizers are parallel.

The operation of nematic LCDs is based on the polarization of the light [19]. In fact, the first polarizer filters the unpolarized light and only the light component with the same polarisation is allowed to propagate through the LCD. While propagating through the LC layer, the light polarization varies depending on the strength of the applied electrical field. Then, two states can be observed, at the second polarizer:

- Clear (Open) state, where the second polarizer has the same polarization direction as the propagating light allowing it to pass.
- Dark (Close) state, where the second polarizer has a different polarization direction from the propagating light blocking it.

These two states are also known as ON and OFF states indicating the presence and absence of an applied voltage in the LC layer. The mapping between the ON/OFF and clear/dark states depends on the LCD's configuration, for example in the case of NW LCD, the clear and dark states correspond, respectively to the OFF and ON states, and vice versa in case of NB LCD. Moreover, this correspondence between states is determined by the mode of the LCD.

Nematic LCDs feature multiple modes distinguished by the molecules alignment and orientation of the LC layer. The most commonly used modes in switchable glass technologies include mainly the twisted nematic (TN) mode, and the untwisted modes namely optically compensated bend (OCB) mode, vertically aligned (VA) mode and electrically controlled birefringence (ECB) mode [19], [21], [22]. In general, the TN mode is one of the most commonly used modes in industry for display and light modulation purposes. Meanwhile, the OCB mode that is also called the "Pi-cell," is considered as the fastest LCD mode [23], while the VA mode is known to have the highest contrast [24]. In terms of switching times, contrast and energy consumption, each mode can have different performances depending on the technology and manufacturer's design.

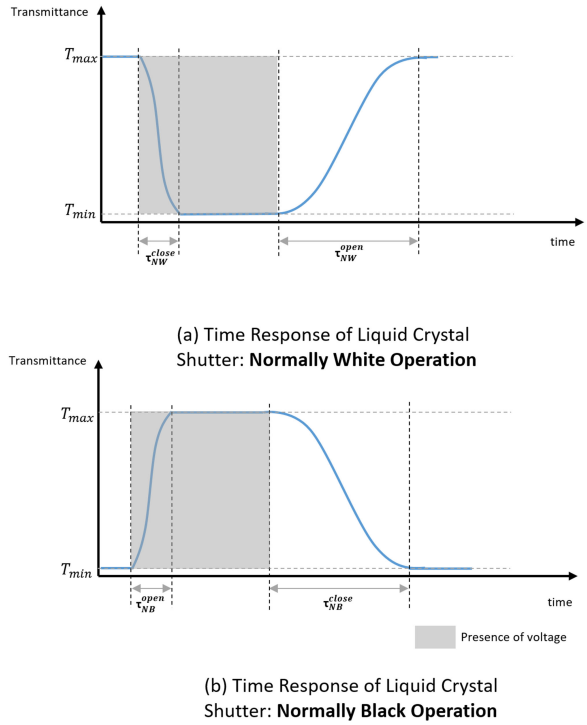

Fig. 3. Time responses of liquid crystal shutters: (a) NW operation and (b) NB operation [11].

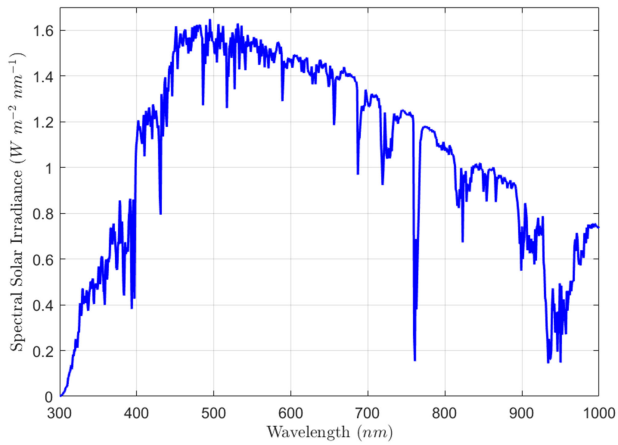

Fig. 4. Spectral Solar irradiance for bandwidth of interest $\lambda = 300 - 1000$ nm.

C. Modeling of a Single-Cell LCD

The mathematical modeling of a single-cell LCD can be realized on two levels; light intensity transmission and time response function.

1) Light Intensity Transmission: This model describes the light transmission through the shutter operating in ON or OFF states. It is not time-dependent and it is mainly governed by the properties of the LC layer as well as the wavelength λ of incident light and the applied voltage V. The modeling differs based on the LCD mode where the twisted modes feature a light transmission that depends mainly on the twist angle Φ, initially equal to $90°$ in the OFF state [25], [26], while untwisted nematic LC cells (ECB, OCB and VA) have a transmission controlled by

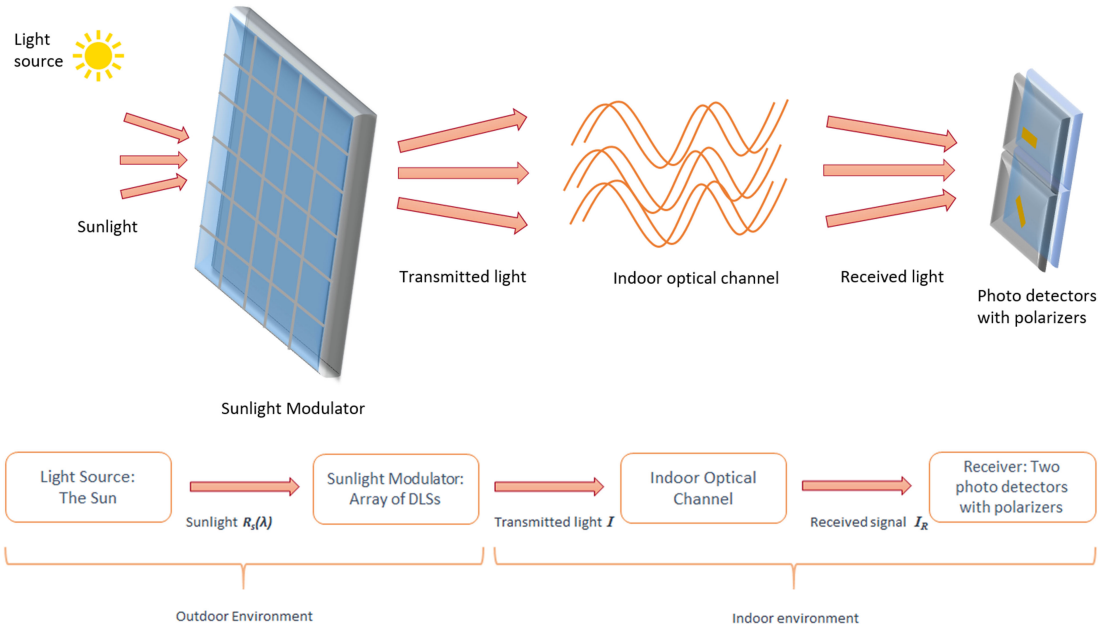

Fig. 5. General overview of the system.

the birefringence of the LC layer [27], [28]. The light intensity transmission is expressed as follows [19],

- Untwisted nematic LCDs

  Case of NW configuration:

$$T(\lambda) = T_0 \sin^2(\delta/2), \tag{2}$$

  Case of NB configuration:

$$T(\lambda) = T_0 \cos^2(\delta/2), \tag{3}$$

- Twisted nematic LCDs

  Case of NB configuration:

$$T(\lambda) = T_0 \frac{\sin^2\left(\frac{\pi}{2}\sqrt{1+u^2}\right)}{(1+u^2)}, \tag{4}$$

  Case of NW configuration:

$$T(\lambda) = T_0 \left[1 - \frac{\sin^2\left(\frac{\pi}{2}\sqrt{1+u^2}\right)}{(1+u^2)}\right], \tag{5}$$

where T_0 is the light intensity, $\delta = \frac{2\pi d\Delta n}{\lambda}$ and $u = \frac{\delta}{2\Phi}$ are known as the phase retardation and the Mauguin parameter of the LC cell, respectively. Δn and d are the LC's birefringence and thickness, and λ is the wavelength of the incoming light. The values of δ and u vary according the strength of the applied voltage V[1] allowing a maximum or minimum transmission.

2) Time Response Function: It characterizes the temporal light transmittance variations of a shutter during opening and closing times. This modeling is common for all LCD modes and has symmetric functions in case of NW and NB operations as illustrated in Fig. 3. During their opening and closing times, LC shutters function similar to charging and discharging of capacitor performance [17]. On one hand, the closing of a single cell LCD of an NW configuration, Fig. 3(a), can be approximated as a decaying exponential ($\exp(-\beta_{\mathrm{NW}_1} t)$), which corresponds to the discharging of a capacitor. Meanwhile, the opening of an NW LCD cell varies similarly to the charging of a capacitor with ($1 - \exp(-\beta_{\mathrm{NW}_2} t)$) as the time response function. On the other hand, in case of NB configuration [Fig. 3(b)], the LCD's response has a decaying exponential behavior ($\exp(-\beta_{\mathrm{NB}_1} t)$), during the closing time and follows a ($1 - \exp(-\beta_{\mathrm{NB}_2} t)$) trend during the opening time. β_{NW_1}, β_{NW_2}, β_{NB_1} and β_{NB_2}, are the time constants indicating the exponential growth or decay rate, and depend on the opening and closing times of the LCD.

III. Sunlight Communication System

The sunlight communication system is displayed in Fig. 5 showing the propagation of sunlight from the outdoors to the indoors, passing through the smart glass containing sunlight modulator composed of an array of DLSs. After its modulation, the light travels in the indoor environment to reach the receiver consisting of two photo detectors equipped with polarizers having different polarization directions. Owing to their simplicity, energy efficiency and high bandwidth, avalanche photodiodes (APD) are suitable detectors for our application.

A. Solar Irradiance

The spectral solar irradiance refers to the solar energy per unit area per wavelength, measured outside the Earth atmosphere or at its surface. It depends on multiple factors including weather

[1]We note that the relation between the applied voltage and the phase retardation for untwisted modes, and the Mauguin parameter for TN modes are not simple involving numerical computations. Appendix-B and Appendix-D of [19] provides details about the evaluation of the transmission of untwisted LCDs and TN LCDs for a given voltage, respectively.

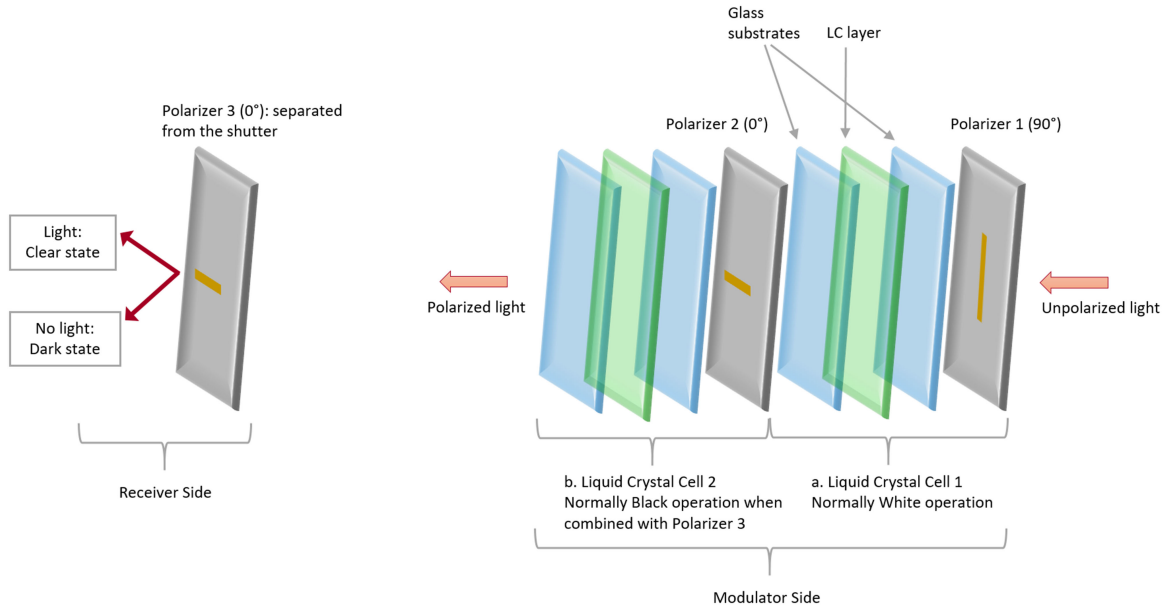

Fig. 6. Proposed design of DLS.

conditions, location, day of the year and time of the day [29]. As a result, defining a generalized simple mathematical model for the spectral solar irradiance is a difficult task. Thus, standard reference spectra have been established to aid researchers to approximate the solar irradiance particularly enabling a fair comparison of the performance of photovoltaic devices developed by different academic and industrial parties.

The standard reference spectra of the American Society for Testing and Materials (ASTM) G-173-03 was developed for terrestrial use and generated using the simple model of the atmospheric radiative transfer of sunshine (SMARTS) under specific conditions averaged for the United States (US) over a period of one year [30].

Using the data provided by the US department of energy / NREL / ALLIANCE [30], we plot the spectral solar irradiance for a range of wavelength $\lambda = 300 - 1000\ nm$ as shown in Fig. 4. Such bandwidth has been chosen to accommodate the capabilities of the photo detectors as most avalanche photodiodes can only detect photons with wavelength $\lambda \in [300 - 1000\ nm]$. Then, we split the data into two sets based on the wavelength range and we fit a linear regression model to each set to determine an approximated function for the irradiance $R_s(\lambda)$ in $Wm^{-2}nm^{-1}$ which can be written as

$$R_s(\lambda) = \begin{cases} a_1\lambda + b_1, & 300nm \leq \lambda \leq 500nm \\ a_2\lambda + b_2, & 500nm \leq \lambda \leq 1000nm \end{cases}, \quad (6)$$

where $a_1 = 0.0087$, $a_2 = -0.0023$, $b_1 = -2.5549$ and $b_2 = 2.8238$ are the models coefficients computed numerically using MATLAB.

B. Dual-Cell Liquid Crystal Shutter Design

Inspired by the time response of the LCs, we stack two liquid crystal shutters with oppositely NW and NB operations. The shutter is composed of two LC cells and three polarizers. Each cell is formed by an LC layer sandwiched between two glass substrates. The first cell ($a.$ in Fig. 6) is placed between two perpendicular polarizers (Polarizer 1 and Polarizer 2). Meanwhile, the second cell ($b.$ in Fig. 6) uses the second polarizer of cell 1 (Polarizer 2) as its back polarizer while its front polarizer (Polarizer 3) is parallel to Polarizer 2. The latter is detached from the shutter and moved to the receiver side permitting the adoption of a polarization-based modulation and aiding in flickering effect mitigation. We refer to this design in Fig. 6 as DLS.

C. Bits Pulse Waves Design

The bits pulse waves are illustrated in Fig. 7. On one hand, to send a bit "1" [Fig. 7(a)], the DLS opens allowing the sunlight to propagate through both NB and NW cells, which yields maximum light transmission for a time period T to be captured by the photo detector at the receiver side. After that, the DLS closes. On the other hand, to transmit a bit "0" [Fig. 7(b)], the DLS blocks the light for the whole symbol duration T_{sym} defined as the sum of the opening and closing times, i.e., $\tau_{\text{NB}}^{\text{open}}$ and $\tau_{\text{NW}}^{\text{close}}$, and the period T as follow,

$$T_{\text{sym}} = \tau_{\text{NB}}^{\text{open}} + \tau_{\text{NW}}^{\text{close}} + T. \quad (7)$$

It is worth to note that $\tau_{\text{NB}}^{\text{open}}$ and $\tau_{\text{NW}}^{\text{close}}$ are material-dependent parameters, while the period T is a tunable parameter that can be adjusted by properly controlling the amount of applied voltages on both NB and NW cells.

Moreover, by properly controlling each cell independently, i.e., different voltage values can be applied to each cell simultaneously, the proposed design of DLS (Fig. 6) provides fast and symmetrical switching times. Firstly, the response times asymmetry, which characterizes single-cell LCDs, can be mitigated by setting $\tau_{\text{NW}}^{\text{close}} = \tau_{\text{NB}}^{\text{open}}$. In fact, the symmetry of switching times

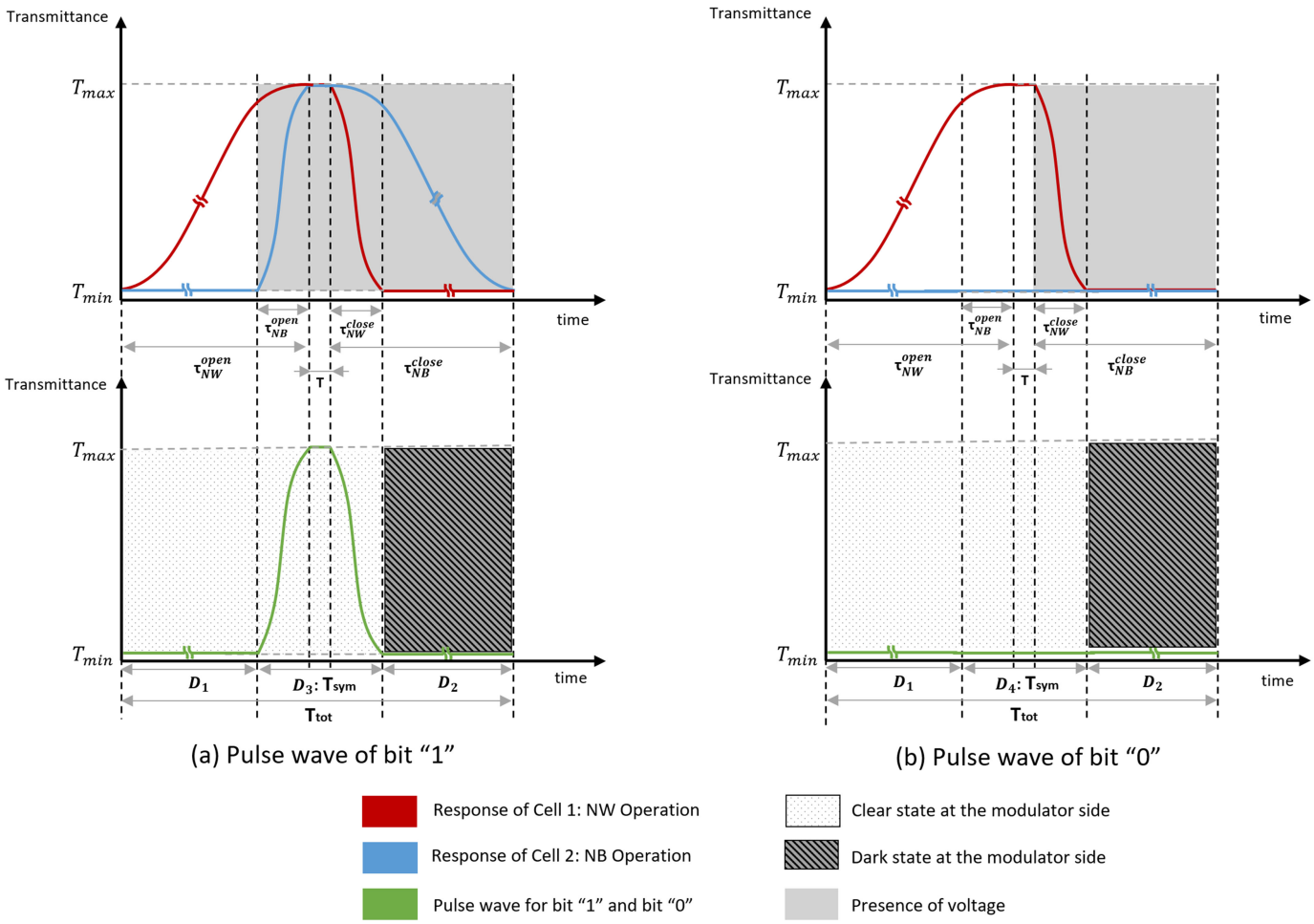

Fig. 7. Pulse waves: (a) bit "1" and (b) bit "0".

offered by our dual-cell design can be observed by the pulse wave of bit "1" in Fig. 7(a). On one hand, the opening time of the DLS (time to switch from minimum to maximum transmission) corresponds to the opening time $\tau_{\text{NB}}^{\text{open}}$ of Cell 2 (NB operation). On the other hand, the closing time of the DLS (time to switch from maximum to minimum transmission) is the closing time $\tau_{\text{NW}}^{\text{close}}$ of Cell 1 (NW operation). Secondly, for conventional LC shutters, the closing time of NW cells is shorter than its opening time and vice versa in case of NB cells. Thus, our dual-cell design leverages the fast times of each cell (opening time of the NB cell and closing time of the NW cell) creating a fast dual-cell liquid crystal shutter.

Another advantage of our DLS design is the elimination of ISI. The DLS cannot modulate the incoming light (*inactive state*) due to the opening and closing times of Cell 1 and Cell 2 respectively, for a time period of $T_{\text{off}} = T_{\text{tot}} - T_{\text{sym}}$, where the total duration T_{tot} is

$$T_{\text{tot}} = \tau_{\text{NW}}^{\text{open}} + \tau_{\text{NB}}^{\text{close}} + T \tag{8}$$

During this time (T_{off}), a DLS allows only a minimum transmission (almost zero) permitting other DLSs to transmit data without interference. In fact, since we control each cell independently to design the bits pulse waves in Fig. 7, we have four time intervals D_j, $j = 1 \ldots 4$ during which different combinations of transmission levels ($T_{\max}$ or $T_{\min}$) of cell 1 and cell 2 are observed, corresponding to the ON and OFF states of each cell:

- Time interval D_1 (first part of T_{off} in Fig. 7): while cell 1 (NW) is opening and the transmittance is increasing, the light passes through the second cell at the modulator side, then it is blocked by the third polarizer at the receiver side because of the OFF state of cell 2 (NB).
- Time interval D_2 (second part of T_{off} in Fig. 7): when cell 2 (NB) is closing, the light is blocked by the first cell (NW) in the ON state forcing the modulator into a dark state and preventing light from reaching neither cell 2 nor the receiver.
- Time interval D_3 [T_{sym} when bit "1" is transmitted in Fig. 7(a)]: when cell 1 in the OFF state and cell 2 in the ON state, the light propagates through both cells at the modulator and receiver sides allowing maximum intensity to reach the photo detector.
- Time interval D_4 [T_{sym} when bit "0" is transmitted in Fig. 7(b)]: when both cells in the OFF state, the light passes through both cells at the modulator side, then it is blocked by the polarizer 3 at the receiver allowing only a minimum intensity to reach the photo detector.

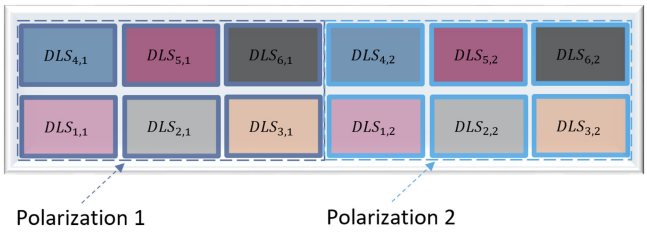

Fig. 8. Sunlight modulator.

Thus, the proper design of the DLS and the pulse waves removes the ISI. Additionally, it enables a flicker-free communication by ensuring a constant average light intensity. This can be achieved by guaranteeing that cell 1 functions similarly when either bits is sent, which makes the dark state at the modulator side appear for the same time interval D_2 during the transmission of bit "1" and bit "0". Therefore, the benefits of the DLS and the pulse waves design include:

- Offering fast and symmetrical opening and closing times.
- Ensuring flicker-free communication.
- Allowing the use of a polarization-based modulation.
- Removing inter-symbol interference.

D. Sunlight Modulator Design

The Sunlight Modulator is composed of an array of DLS pairs which can be arranged in different manners. Fig. 8 illustrates one possible setup having two groups of 6 pixels. First, we exploit the polarization domain where each pair of DLSs transmit data simultaneously over the orthogonal polarization channels 1&2. This simultaneous operation is indicated by the pair's index, for example the pair ($DLS_{1,1}$, $DLS_{1,2}$) are expected to send data during the same T_{sym}. Further, to improve the data rate, each group of pixels uses a time divison multiplexing (TDM) technique over its corresponding channel.

1) Polarization-Based Modulation: We profit from the light polarization property to alleviate the flickering effect and improve the data rate where we base our modulation on the polarization based QAM (PQAM) scheme introduced in [12]. Our proposed pair of DLS pixels has two polarizers with a relative polarization angle of $45°$, as presented in Fig. 9(a). Polarizer 1 of the first DLS (the upper pixel) features an axis having $\theta_{11} = 90°$ angle with the horizontal direction while it has an angle of $\theta_{12} = 45°$ in case of the second pixel. The unpolarized Sunlight propagates through the LC cells of each DLS to emerge as a polarized light having two possible polarization angles depending of the transmitted bit. For example, if bit "1" is sent by DLS 1, then the output signal would have a polarization angle $\phi_1 = 0°$ whereas if bit "0" is transmitted, then ϕ_1 would be equal to $90°$. Equivalently, when DLS 2 sends bit "1," the angle of the polarized light would be $\phi_2 = -45°$ and when it transmits bit "0," ϕ_2 becomes $45°$.

Then, once the polarized light reaches the receiver side and passes through the third polarizers with polarization angles $\theta_{31} = 0°$ and $\theta_{32} = -45°$, the intensity of the polarized signal at the $k^{\text{th}} = 1, 2$ receiver can be determined using (1), which reduces to, for $0 \leq t \leq T_{\text{sym}}$,

$$s_k(t,\lambda) = \begin{cases} p_1(t,\lambda)\cos^2(\phi_k - \theta_{3k}), & b_k = 1 \\ p_0(t,\lambda)\cos^2(\phi_k - \theta_{3k}) + p_0(t,\lambda), & b_k = 0 \end{cases}, \tag{9}$$

where $\phi_k \in \{0°, 90°, 45°, -45°\}$ is the polarization angle of the signal when bit $b_k = 0, 1$ is sent by the $k^{\text{th}} = 1, 2$ DLS pixels. As mentioned in Section II-A, practical polarizers allows a portion of light to passe through and because Malus's law assumes ideal polarizers, the term $p_0(t,\lambda)$ in (9) takes into account this minimum transmission occurring when bit "0" is sent. Then, the intensity $s_k(t,\lambda)$ can simplified and it becomes

$$\begin{aligned} s_k(t,\lambda) &= (p_1(t,\lambda) - p_0(t,\lambda))\cos^2(\phi_k - \theta_{3k}) + p_0(t,\lambda) \\ &= (p_1(t,\lambda) - p_0(t,\lambda))\frac{\cos 2(\phi_k - \theta_{3k}) + 1}{2} + p_0(t,\lambda) \\ &= \frac{p_1(t,\lambda) - p_0(t,\lambda)}{2} Q_k + \frac{p_1(t,\lambda) + p_0(t,\lambda)}{2}, \end{aligned} \tag{10}$$

where $Q_k = \cos 2(\phi_k - \theta_{3k})$ describes the polarization channels and can be further examined to prove the channels orthogonality as demonstrated in [12]. In fact, Q_k can be written as the result of a dot product as follows

$$\begin{aligned} Q_k &= \cos 2(\phi_k - \theta_{3k}) \\ &= \cos 2\phi_k \cos 2\theta_{3k} + \sin 2\phi_k \sin 2\theta_{3k} \\ &= \begin{bmatrix} \cos 2\phi_k & \sin 2\phi_k \end{bmatrix} \begin{bmatrix} \cos 2\theta_{3k} \\ \sin 2\theta_{3k} \end{bmatrix}. \end{aligned} \tag{11}$$

Now, inspecting the terms Q_1 and Q_2 and replacing the angles θ_{31} and θ_{32} by their values, we have

$$\begin{aligned} Q_1 &= \cos 2(\phi_1 - \theta_{31}) \\ &= \begin{bmatrix} \cos 2\phi_1 & \sin 2\phi_1 \end{bmatrix} \begin{bmatrix} \cos 2\theta_{31} \\ \sin 2\theta_{31} \end{bmatrix} \\ &= \begin{bmatrix} \cos 2\phi_1 & \sin 2\phi_1 \end{bmatrix} \begin{bmatrix} 1 \\ 0 \end{bmatrix}. \end{aligned} \tag{12}$$

$$\begin{aligned} Q_2 &= \cos 2(\phi_2 - \theta_{32}) \\ &= \begin{bmatrix} \cos 2\phi_2 & \sin 2\phi_2 \end{bmatrix} \begin{bmatrix} \cos 2\theta_{32} \\ \sin 2\theta_{32} \end{bmatrix} \\ &= \begin{bmatrix} \cos 2\phi_2 & \sin 2\phi_2 \end{bmatrix} \begin{bmatrix} 0 \\ -1 \end{bmatrix}. \end{aligned} \tag{13}$$

It is clear that the vectors $V_{\text{pol}_1} = [1, 0]^T$ and $V_{\text{pol}_2} = [0, -1]^T$ are orthogonal since their dot product is null. Thus, the two vectors define an orthogonal basis formed by the receivers with polarizers having their polarization directions differ by an angle of $45°$. Also, Fig. 9(b) illustrates the relation between the 4-PQAM symbols and the polarization angles of the optical signal where each symbol is formed by two bits transmitted using the pair of DLS pixels, and it is represented by a point having the coordinates $(\cos(2\phi_1), \sin(2\phi_2))$ in the orthogonal basis $\{V_{\text{pol}_1}, V_{\text{pol}_2}\}$.

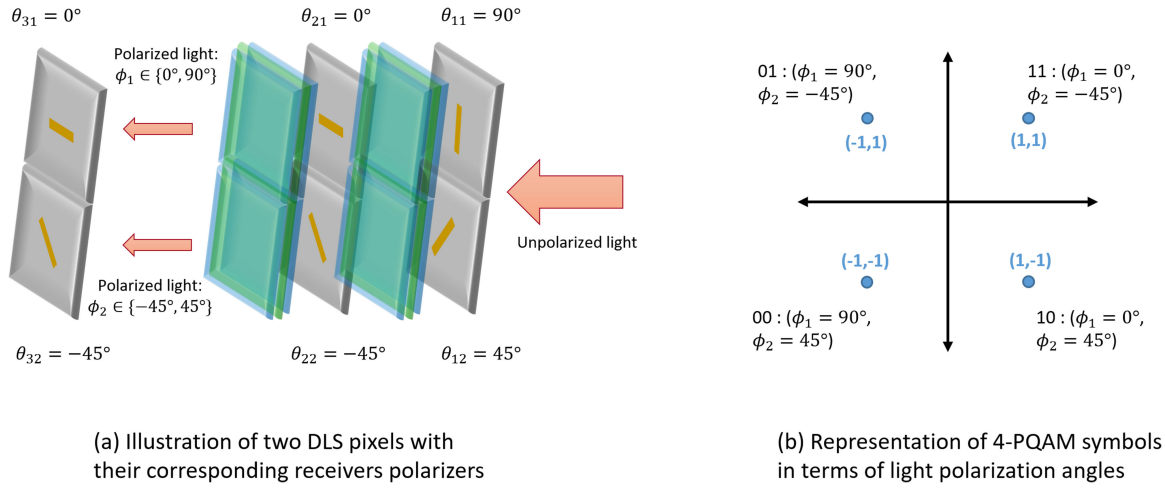

Fig. 9. Illustration of the polarization modulation technique with two DLS pixels.

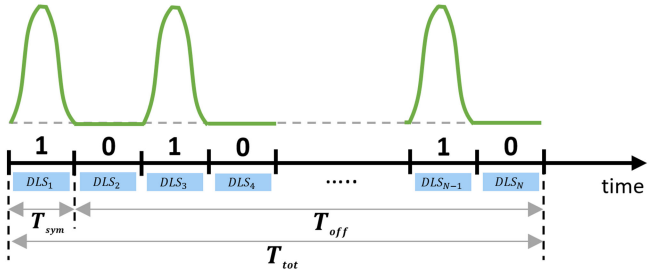

Fig. 10. Illustration of the TDM data transmission.

The modulation is characterized by its robustness to angular misalignment between the modulator and the receiver [12]. Assuming that the receiver's mobility causes $\Delta\xi$ difference of polarization angle, then the constellation will be rotated by $2\Delta\xi$ which can be corrected by conventional methods.

2) Time Division Multiplexing: We employ a time divison multiplexing (TDM) technique to utilize the time domain as illustrated in Fig. 10. Because the DLS enters an *inactive state* for a time length of T_{off}, other DLS pixels should be in *active states* such that the inactive time T_{off} of a pair of DLS pixel can be used to transmit information until the initial DLS pair becomes active again. To fully use the entire time frame and the two polarization channel, the total number of pixels required is $N_{\text{pixel}} = 2 * N_{\text{TDM}}$ where $N_{\text{TDM}} = \lfloor T_{\text{tot}}/T_{\text{sym}} \rfloor$ is the number of pixels needed to achieve TDM over the total duration.

IV. Mathematical Modeling

A. Modeling of a Single Dual-Cell Liquid Crystal Shutter

Using the single-cell light transmission models presented in Section II-C, we derive the transmission of the proposed dual-cell shutter. This model expresses the double attenuation in terms of light intensity caused by the NW and NB cells. Considering the third polarizer at the receiver side, the DLS light transmission is given by:

Untwisted modes:

$$T_{\text{UTN}}(\lambda) = T_0(\lambda) \underbrace{\sin^2(\delta_1/2)}_{\text{Transmittance of cell 1}} \underbrace{\cos^2(\delta_2/2)}_{\text{Transmittance of cell 2}} . \quad (14)$$

Twisted modes:

$$T_{\text{TN}}(\lambda) = T_0(\lambda) \underbrace{\left[1 - \frac{\pi^2}{4}\text{sinc}^2\left(\frac{\pi}{2}\sqrt{1+u_1^2}\right)\right]}_{\text{Transmittanceofcell1}} \underbrace{\left[\frac{\pi^2}{4}\text{sinc}^2\left(\frac{\pi}{2}\sqrt{1+u_2^2}\right)\right]}_{\text{Transmittanceofcell2}} . \quad (15)$$

where $T_0(\lambda) = \alpha_1\alpha_2\alpha_3 A_{\text{DLS}} R_{\text{s}}(\lambda)$ with A_{DLS} denoting the DLS area, α_1, α_2 and $\alpha_3 \in [0, 1]$ representing the transmittance of the three polarizers. lso, δ_i and u_i, $i = 1, 2$ are the phase retardation and the Mauguin parameter of cell 1 and 2, respectively, defined as follows:

$$\delta_i = \frac{2\pi d_i \Delta n_i}{\lambda} \quad \text{and} \quad u_i = \frac{\pi d_i \Delta n_i}{\lambda \Phi}, \quad i = 1, 2. \quad (16)$$

They capture the characteristics of each LC cell of the device including the LC layer thickness (d_i) and its wavelength sensitivity (λ). Their values vary according the strength of the applied voltage on each cell V_1, V_2 such that different light intensities are captured by the photo detector during each time intervals $D_j, j = 1, \ldots, 4$.

The time response of the proposed DLS design, can be characterised by the opening of a NB LCD which a $(1 - \exp(-t))$ trend and the closing of a NW LCD with a decaying exponential $(\exp(-t))$. Thus, the temporal pulse wave for specific λ for a "1" transmission is expressed as,

$$p_1(t, \lambda) = \begin{cases} T_D(\lambda)(1 - \exp(-\beta_1 t)) + T_{\min}(\lambda), & 0 \le t \le \tau_{\text{NB}}^{\text{open}} \\ T_{\max}(\lambda), & \tau_{NB}^{\text{open}} \le t \le \tau \\ T_D(\lambda)\exp(-\beta_2(t-\tau)) + T_{\min}(\lambda), & \tau \le t \le T_{\text{sym}} \end{cases}, \quad (17)$$

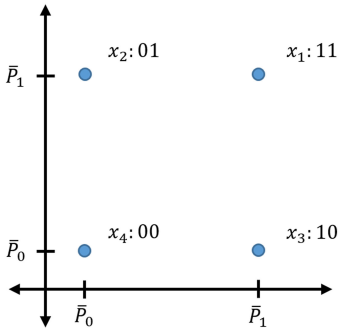

Fig. 11. Representation of 4-PQAM symbols in terms of average light intensities.

where $T_D(\lambda) = T_{\max}(\lambda) - T_{\min}(\lambda)$, $\beta_1 = \frac{5}{\tau_{\text{NB}}^{\text{open}}}$ and $\beta_2 = \frac{5}{\tau_{\text{NW}}^{\text{close}}}$ are determined numerically to properly approximate the time responses in Fig. 3, and $\tau = T_{\text{sym}} - \tau_{\text{NW}}^{\text{close}} = \tau_{\text{NB}}^{\text{open}} + T$. On the other hand, when "0" is sent, the pulse wave is a constant over the symbol duration and it is given by

$$p_0(t,\lambda) = T_{\min}(\lambda), \qquad \text{for } 0 \le t \le T_{\text{sym}}, \tag{18}$$

where $T_{\max}(\lambda)$ and $T_{\min}(\lambda)$ are the maximum and minimum light intensities, defined in case of untwisted nematic cells as,

$$T_{\max}(\lambda) = T_0(\lambda)\sin^2(\delta_{1,\max}/2)\cos^2(\delta_{2,\max}/2), \tag{19}$$

$$T_{\min}(\lambda) = T_0(\lambda)\sin^2(\delta_{1,\min}/2)\cos^2(\delta_{2,\min}/2), \tag{20}$$

where $\delta_{i,\max}$ and $\delta_{i,\min}$ are the phase retardations of the $i^{\text{th}} = 1, 2$ cell yielding to maximum and minimum transmission of the DLS[2]. Therefore, the overall pulse wave of a single pixel DLS becomes

$$p(t,\lambda) = \begin{cases} p_1(t,\lambda), & \text{for bit = 1} \\ p_0(t,\lambda), & \text{for bit = 0} \end{cases}, \quad 0 \le t \le T_{\text{sym}}. \tag{21}$$

B. Sunlight Modulator Modeling

Since the photo detectors, at the receiver side, cannot capture the polarization of optical signals and instead can detect the light intensity, a representation of the 4-PQAM symbols in terms of average light intensities (Fig. 11) is needed for the detection process. Hence, using (10), the intensity of the joint signal can be expressed as

$$\begin{aligned}\mathbf{S}(t,\lambda) &= (p_1(t,\lambda) - p_0(t,\lambda))\begin{bmatrix}\cos^2(\phi_1 - \theta_{31}) \\ \cos^2(\phi_2 - \theta_{32})\end{bmatrix} + p_0(t,\lambda) \\ &= (p_1(t,\lambda) - p_0(t,\lambda))\begin{bmatrix}\cos^2(\phi_1) \\ \cos^2(\phi_2 + 45^\circ)\end{bmatrix} + p_0(t,\lambda).\end{aligned} \tag{22}$$

Then, the average signal intensity $\bar{\mathbf{S}}_m(\lambda)$ corresponding to the transmitted symbol x_m, $m = 1, 2, 3, 4$, as shown in Fig. 11, can be written as

$$\bar{\mathbf{S}}_m(\lambda) = \left(\bar{P}_1(\lambda) - \bar{P}_0(\lambda)\right)\begin{bmatrix}\cos^2((m-1)90^\circ) \\ \cos^2\left(\left[m - \frac{1}{2}(3+(-1)^m)\right]45^\circ\right)\end{bmatrix} + \bar{P}_0(\lambda), \tag{23}$$

where $\bar{P}_1(\lambda)$ and $\bar{P}_0(\lambda)$ are the average light intensities over the symbol duration T_{sym} when bit "1" and "0" are transmitted, respectively, and given by

$$\begin{aligned}\bar{P}_1(\lambda) &= \int_0^{T_{\text{sym}}} p_1(t,\lambda)\,dt \\ &= \left(T + 5\tau_{\text{NW}}^{\text{close}} - 4\tau_{\text{NB}}^{\text{open}}\right)T_{\max}(\lambda) \\ &\quad + \left(5\tau_{\text{NB}}^{\text{open}} - 4\tau_{\text{NW}}^{\text{close}}\right)T_{\min}(\lambda) \\ &\quad + \frac{5\left(\tau_{NB}^{open} - \tau_{\text{NW}}^{\text{close}}\right)}{e^{1/5}}(T_{\max}(\lambda) - T_{\min}(\lambda)).\end{aligned} \tag{24}$$

Then, by having $\tau_{\text{NW}}^{\text{close}} = \tau_{\text{NB}}^{\text{open}}$, we guarantee the symmetry of the LC shutter, $\bar{P}_1(\lambda)$ can be simplified to

$$\bar{P}_1(\lambda) = TT_{\max}(\lambda) + \tau_{\text{NW}}^{\text{close}}(T_{\max}(\lambda) + T_{\min}(\lambda)), \tag{25}$$

and $\bar{P}_0(\lambda)$ becomes

$$\begin{aligned}\bar{P}_0(\lambda) &= \int_0^{T_{\text{sym}}} p_0(t,\lambda)\,dt \\ &= T_{\text{sym}}T_{\min}(\lambda).\end{aligned} \tag{26}$$

Furthermore, as explained in Section III-D, a TDM method is used to exploit the total time period T_{tot} such that for each symbol duration $T_{\text{sym}} \in [0, T_{\text{tot}}]$, only one DLS pair is transmitting data. Thus, during each T_{sym}, the transmitted signal by one DLS pair is

$$\begin{aligned}X_n(t) &= \mathbf{S}(t - (n-1)T_{\text{sym}}, \lambda), \\ &\quad (n-1)T_{\text{sym}} \le t \le nT_{\text{sym}}, \;\; n = 1, 2 \ldots N_{\text{TDM}},\end{aligned} \tag{27}$$

where N_{TDM} represents the number of DLS pixels needed to totally utilize the available duration.

C. Indoor Channel Modeling

To comprehend the indoor optical channel, we first examine the incidence of the sunlight on the modulator surface. In Fig. 12, the incoming Sun rays are assumed to have the same incidence angle ψ_{inc} with the normal to the modulator surface regardless of the Sun's position. The variation of the Sun's location over time is captured by the variation of solar irradiance. The incidence angle ψ_{inc} is equal to half of the apparent angular diameter of the Sun, defined as the angle that the Sun makes when observed at a specific distance, which is approximated as $32' \approx 0.5^\circ$ [31].

After passing through the DLS layers, the Sun rays emerges with a divergence angle $\psi_{\text{div}} = \psi_{\text{inc}}$, this is due to Snell's law where the light propagates from the air, through the different material layers of the DLS to the air again maintaining the same angle [32]. Therefore, assuming a circular DLS pixel, its footprint area A_{FP} on the APD's plane is given by

$$A_{\text{FP}_k} = \pi[r_{DLS_k} + d_k \tan(\psi_{\text{div}})]^2, \tag{28}$$

[2]Similarly for TN cells the $T_{\max}(\lambda)$ and $T_{\min}(\lambda)$ are found by replacing the Mauguin parameter by its maximum and minimum values.

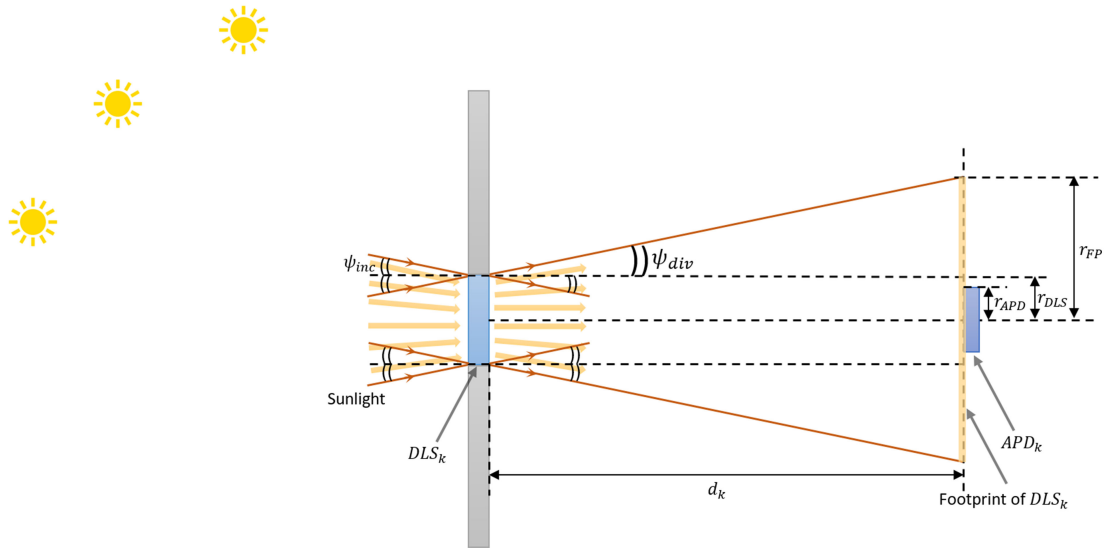

Fig. 12. Geometry of the indoor LOS optical link.

where the divergence angle $\psi_{\text{div}} \approx 16' \approx 0.266667°$, r_{DLS_k} is the radius of the k^{th} DLS and d_k is the distance between the DLS's and the APD's planes. Hence, assuming a perfect alignment where the APD detection area is completely covered by the footprint of the DLS (FP), the channel gain h_k of the Line of Sight (LOS) optical link between $k^{\text{th}} = 1, 2$ DLS and APD is given by

$$h_k = g(\psi_k)\frac{A_{APD_k}}{A_{FP_k}}, \tag{29}$$

where A_{APD_k} is the APD detection area and $g(\psi_k)$ is the concentrator gain, expressed as [33]

$$g(\psi_k) = \begin{cases} \frac{n_c^2}{\sin^2 \psi_{\text{F}_k}}, & 0 \le \psi_k \le \psi_{\text{F}_k} \\ 0, & \psi_k > \psi_{\text{F}_k} \end{cases}, \tag{30}$$

where $\psi_{\text{F}_k} \le 90°$ denotes the receiver's field of view and n_c is the refractive index of the concentrator.

Nonetheless, the complete inclusion of the APD detection area in the DLS footprint, as shown in Fig. 12, is a particular case which can be achieved in various scenarios. For example, at short distances, the APD can be positioned in a perfect alignment with a certain DLS [Fig. 13(a)] making the footprint area equal to the DLS area ($r_{FP_{n,k}} = r_{DLS_{n,k}}, n = 1, 2 \ldots N_{\text{TDM}}$), resulting into 100% intersection between its area and the $DLS_{2,1}$ footprint and a 0% intersection with other footprints. A more general case can be observed in Fig. 13(b) where the APD's area is partially covered by different DLS footprints. Then, as the APD moves farther from the modulator's plane, the radius of the footprints increases allowing more intersection with the detection area. For instance, at medium distances, as illustrated in Fig. 13(c), the area is fully covered by the footprint of $DLS_{2,1}$, while it is partially covered by other footprints ($FP_{4,1}$). Meanwhile at longer distances, the APD can be localised such that its area is completely included in multiple footprints [Fig. 13(d)]. To simplify the illustrations in this section and thanks to the symmetry of the two groups (Fig. 8), we focus on the group of pixels transmitting over the first polarization channel ($DLS_{n,1}$). We also note that there is no interference between the different footprints since only one DLS pair would be operating during each T_{sym} as explained in previous sections.

Therefore, the general channel gain h_k capturing the different cases is given by

$$h_k = \begin{cases} 0, & d_{APD_k - DLS_{n,k}} \ge r_{FP_{n,k}} + r_{APD_k} \\ g(\psi_k)\frac{A_{APD_k}}{A_{FP_{n,k}}}, & d_{APD_k - DLS_{n,k}} \le r_{FP_{n,k}} - r_{APD_k} \\ g(\psi_k)\frac{A_{inter_{n,k}}}{A_{FP_{n,k}}}, & \text{otherwise} \end{cases}, \tag{31}$$

where $A_{\text{inter}_{\text{n,k}}}$ is the intersection area between the detection area of the APD and the n^{th} footprint, expressed as

$$\begin{aligned} A_{inter_{n,k}} &= r_{FP_{n,k}}^2 \cos^{-1}\left(\frac{\epsilon_1}{r_{FP_{n,k}}}\right) - \epsilon_1\sqrt{r_{FP_{n,k}}^2 - \epsilon_1^2} \\ &\quad + r_{APD_k}^2 \cos^{-1}\left(\frac{\epsilon_2}{r_{APD_k}}\right) - \epsilon_2\sqrt{r_{APD_k}^2 - \epsilon_2^2}, \\ \text{where} \quad \epsilon_1 &= \frac{r_{FP_{n,k}}^2 - r_{APD_k}^2 + d_{APD_k - DLS_{n,k}}^2}{2d_{APD_k - DLS_{n,k}}}, \\ \epsilon_2 &= d_{APD_k - DLS_{n,k}} - \epsilon_1, \end{aligned} \tag{32}$$

and $d_{APD_k - DLS_{n,k}}$ is the distance between the center of the APD and the center of the n^{th} DLS, given by

$$\begin{aligned} &d_{APD_k - DLS_{n,k}} \\ &= \sqrt{(x_{APD_k} - x_{DLS_{n,k}})^2 + (y_{APD_k} - y_{DLS_{n,k}})^2}, \end{aligned} \tag{33}$$

where (x_{APD_k}, y_{APD_k}) and $(x_{DLS_{n,k}}, y_{DLS_{n,k}})$ are the coordinates specifying the APD and DLS positions. The coordinate system is based on a grid describing the location of each DLS pixel with respect to other pixels is the modulator plane. Since circular DLSs are employed, the minimum distance between adjacent pixels is $2r_{\text{DLS}}$ and the coordinates of each DLS are defined as

$$\begin{aligned} x_{DLS_{n,k}} &= (2x+1)r_{\text{DLS}}, \quad x = 0, 1, \ldots, (X_{\text{TDM}} - 1), \\ y_{DLS_{n,k}} &= (2y+1)r_{\text{DLS}}, \quad y = 0, 1, \ldots, (Y_{\text{TDM}} - 1), \end{aligned} \tag{34}$$

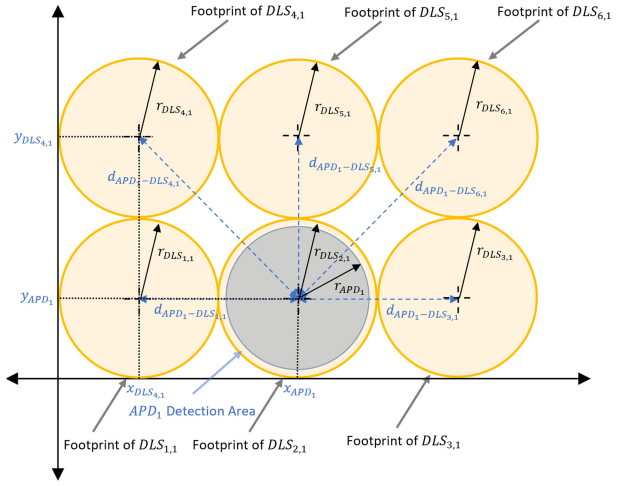

(a) Short distances (perfect alignment of APD_1 and $DLS_{2,1}$)

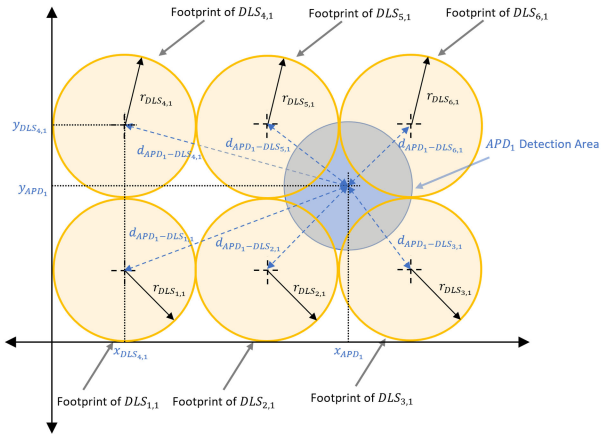

(b) Short distances (no perfect alignment of APD_1 and other $DLS_{n,1}$)

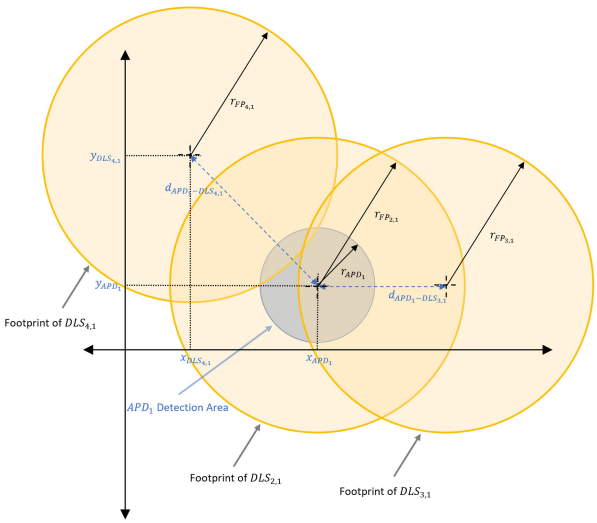

(c) Medium distances (footprints of $DLS_{2,1}$, $DLS_{3,1}$ and $DLS_{4,1}$)

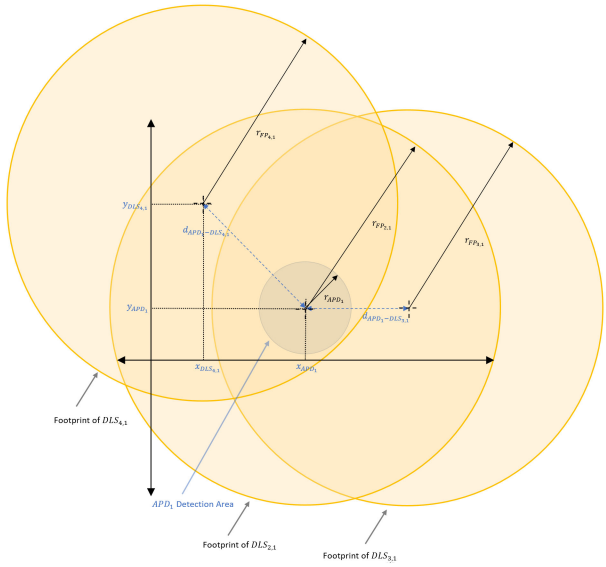

(d) Long distances (footprints of $DLS_{2,1}$, $DLS_{3,1}$ and $DLS_{4,1}$)

Fig. 13. Intersection of $DLS_{n,1}$ footprints and APD_1 detection area at different distances.

where X_{TDM} and Y_{TDM} are the number of DLS pixels placed on the $x-$ axis and $y-$ axis, respectively, such that $N_{\text{TDM}} = X_{\text{TDM}} Y_{\text{TDM}}$.

D. Receiver Modeling

At the receiver side, two APDs equipped with two polaziers are used to detect the transmitted data and the received signal at the $k^{\text{th}} = 1, 2$ APD can be written as follows

$$y_k(t, \lambda) = h_k s_k(t, \lambda) + n_k(t), \qquad 0 \le t \le T_{\text{sym}}, \tag{35}$$

where h_k represents the gain of the indoor LOS channel and n_k is the detection noise. Then, the photocurrent i_k generated by the k^{th} APD during the symbol duration T_{sym} are [33]

$$i_k = I_{p_k} + n_k, \tag{36}$$

where $I_{p_k} = I_{p_k}^{b_k}$ is the average photocurrent generated when bit $b_k = 0, 1$ is transmitted. I_{p_k} encapsulates the average DLS sensitivity and received sunlight intensity over the detectable wavelength band as follows,

$$\begin{aligned} I_{p_k} &= h_k \int_{\lambda_1}^{\lambda_2} \int_0^{T_{\text{sym}}} R_{APD_k}(\lambda) s_k(t, \lambda)\, dt\, d\lambda \\ &= \begin{cases} h_k \int_{\lambda_1}^{\lambda_2} R_{APD_k}(\lambda) \bar{P}_1(\lambda)\, d\lambda, & b_k = 1 \\ h_k \int_{\lambda_1}^{\lambda_2} R_{APD_k}(\lambda) \bar{P}_0(\lambda)\, d\lambda, & b_k = 0 \end{cases}, \end{aligned} \tag{37}$$

where λ_1 and λ_2 are the minimum and maximum detectable wavelength of the Sunlight spectrum, and $R_{APD_k}(\lambda) = \eta_k(\lambda) M_k \frac{q\lambda}{hc}$ is the responsivity of the photodetector with $\eta_k(\lambda)$ and M_k denoting the quantum efficiency and gain of the APD, h, c and q are Planck's constant, speed of light and the electron charge. The random photon counting process of k^{th} APD is accompanied with the shot noise which is the major noise component. Although, it can be modeled by a Poisson distribution and it is usually approximated with a Gaussian distribution, for large numbers of counted photons, having a zero mean and a

variance $\sigma^2_{S_k}$ expressed as [34]

$$\sigma^2_{S_k} = 2q\bar{I}_{p_k} B_k M_k^2 F_k(M_k), \tag{38}$$

where $\bar{I}_{p_k} = p_0 I^0_{p_k} + p_1 I^1_{p_k}$ with p_0 and p_1 are the probabilities of sending bit "0" and "1," B_k and F_k are the bandwidth and excess noise of the APD. The second type of noise is the thermal noise, it is induced by the thermal variations in the electrical circuit [35] and modeled as a zero mean Gaussian process with variance $\sigma^2_{T_k}$ given by [34],

$$\sigma^2_{T_k} = \frac{4K_B T_{APD_k} B_k}{R_{T_k}}, \tag{39}$$

where K_B is Boltzmann's constant, T_{APD_k} and R_{T_k} are the temperature and resistance values. Another source of noise is the electric current generated by the APD in absence of light. Known as the dark current noise, it is also follows a zero mean Gaussian distribution with variance $\sigma^2_{D_k}$ expressed as [34],

$$\sigma^2_{D_k} = 2qI_{D_k} B_k M_k^2 F_k(M_k), \tag{40}$$

where I_{D_k} is the dark current. Hence, the sum of the these noises n_k is modeled as a zero mean Additive White Gaussian Noise (AWGN) having variance of $\sigma^2_{N_k} = \sigma^2_{S_k} + \sigma^2_{T_k} + \sigma^2_{D_k}$.

Single dimension detection: At the step of signal detection, the received signal at each APD can be decoded individually to determine the transmitted bit b_k, then the two bits symbol is formed as $b_1 b_2$. The conditional probability of the generated photocurrent i_k at the k^{th} APD, given the transmitted bit b_k is [33],

$$P_r(i_k|b_k = 0, 1) = \frac{1}{\sqrt{2\pi\sigma^2_{N_k}}} \exp\left(-\frac{(i_k - I^{b_k}_{p_k})^2}{2\sigma^2_{N_k}}\right), \tag{41}$$

Then, assuming that the bit $b_k = 0$ or 1 is transmitted with probability $P_r(b_k) = p_0$ or p_1, the Maximum a Posteriori (MAP) detector is,

$$\begin{aligned}\hat{b}_k &= \arg\max_{b_k}[P_r(b_k) P_r(i_k|b_k)] \\ &= \arg\max_{b_k}[2\sigma^2_{N_k} \ln P_r(b_k) - (i_k - I^{b_k}_{p_k})^2].\end{aligned} \tag{42}$$

In case of transmitting bits with equal probabilities ($P_r(b_k) = p_0 = p_1$), the MAP detector becomes

$$\hat{b}_k = \arg\min_{b_k}\left[\left(i_k - I^{b_k}_{p_k}\right)^2\right]. \tag{43}$$

Joint signal detection: The detection can be conducted jointly in an optimal manner. Using (22), the joint received signal $\mathbf{Y}(t, \lambda)$ can be expressed as,

$$\begin{aligned}\mathbf{Y}(t, \lambda) &= \mathbf{H}\mathbf{S}(t, \lambda) + \mathbf{N} \\ &= \begin{bmatrix} h_1 & 0 \\ 0 & h_2 \end{bmatrix} \begin{bmatrix} s_1(t, \lambda) \\ s_2(t, \lambda) \end{bmatrix} + \begin{bmatrix} n_1 \\ n_2 \end{bmatrix},\end{aligned} \tag{44}$$

where $\mathbf{H}$ and $\mathbf{N}$ are the channel matrix and the noise vector. Then, the average photocurrent jointly generated by the APDs is expressed as,

$$\begin{aligned}\mathbf{I}_m &= \begin{bmatrix} I_{p_1,m} \\ I_{p_2,m} \end{bmatrix} \\ &= \int_{\lambda_1}^{\lambda_2} \int_0^{T_{\text{sym}}} \mathbf{G}(\lambda)\mathbf{S}(t, \lambda)\, dt\, d\lambda \\ &= \int_{\lambda_1}^{\lambda_2} \mathbf{G}(\lambda)\mathbf{S}_m(\lambda)\, d\lambda,\end{aligned} \tag{45}$$

where $\mathbf{G}(\lambda) = \text{diag}(h_k R_{APD_k}(\lambda), k = 1, 2)$.

Since the received signals at each APD are independent, the conditional probability of the jointly generated photocurrents $\mathbf{i} = [i_1 i_2]^T$, given the transmitted symbol x_m is

$$\begin{aligned}P_r(\mathbf{i}|x_m) &= P_r(i_1|x_m) P_r(i_2|x_m) \\ &= \frac{1}{2\pi\sigma_{N_1}\sigma_{N_2}} \exp\left(-\frac{(i_1 - I_{p_1,m})^2}{2\sigma^2_{N_1}} - \frac{(i_2 - I_{p_2,m})^2}{2\sigma^2_{N_2}}\right).\end{aligned} \tag{46}$$

Assuming that the symbol x_m is transmitted with probability $P_r(x_m)$, the MAP detector is

$$\hat{x}_m = \arg\max_{x_m}\left[\ln P_r(x_m) - \frac{(i_1 - I_{p_1,m})^2}{2\sigma^2_{N_1}} - \frac{(i_2 - I_{p_2,m})^2}{2\sigma^2_{N_2}}\right]. \tag{47}$$

If the APDs are characterized by detection noises having the same variance $\sigma^2_{N_1} = \sigma^2_{N_2} = \sigma^2_N$, the conditional probability and the MAP detector become

$$P_r(\mathbf{i}|x_m) = \frac{1}{2\pi\sigma^2_N} \exp\left(-\frac{\|\mathbf{i} - \mathbf{I}_m\|^2}{2\sigma^2_N}\right), \tag{48}$$

$$\hat{x}_m = \arg\max_{x_m}\left[2\sigma^2_N \ln P_r(x_m) - \|\mathbf{i} - \mathbf{I}_m\|^2\right]. \tag{49}$$

Now, assuming that the symbols x_m are equiprobable, the MAP detector is simplified to the Maximum Likelihood (ML) detector

$$\hat{x}_m = \arg\min_{x_m} \|\mathbf{i} - \mathbf{I}_m\|^2. \tag{50}$$

Therefore, taking into account the Time Division Multiplexing (TDM), illustrated in Fig. 10, the received signal over the total duration T_{tot} is

$$\mathbf{Y}_{\text{TDM}}(t, \lambda) = \sum_{n=1}^{N_{\text{TDM}}} \mathbf{Y}(t - (n-1)T_{\text{sym}}, \lambda). \tag{51}$$

V. Performance Analysis

A. Error Probability

To evaluate the communication performance of the system, we derive the error probability (or Bit Error Rate) of the 4-PQAM modulation, using the symbol representation in Fig. 11, as follows

$$P_{\text{error}} = 1 - \left[1 - Q\left(\frac{I_{\text{th}_1}}{\sigma_{N_1}}\right)\right]\left[1 - Q\left(\frac{I_{\text{th}_2}}{\sigma_{N_2}}\right)\right], \tag{52}$$

where $Q(x)$ is the Q-function and I_{th_1} and I_{th_2} are the optimum detection threshold given by

$$I_{th_k} = \frac{I^1_{p_k} - I^0_{p_k}}{2}, \qquad k = 1, 2. \tag{53}$$

If we assume that the pair of DLS pixels and their corresponding pair of APDs have similar characteristics and each pair are sufficiently close, then the noises n_1 and n_2 would have the same variance ($\sigma^2_{N_1} = \sigma^2_{N_2} = \sigma^2_N$) and the channel gains h_1 and h_2 would be identical resulting into $I_{\text{th}} = I_{\text{th}_1} = I_{\text{th}_2}$. Thus, the error probability in (52) can be simplified as

$$P_{\text{error}} = 1 - \left[1 - Q\left(\frac{I_{\text{th}}}{\sigma_N}\right)\right]^2. \tag{54}$$

B. Transmission Data Rate

The design of one pixel of DLS allows the transmission of one bit over the total time duration. So, in terms of achievable data rate, one pixel of DLS can only provide a rate of $R_{\text{DLS}} = 1/T_{\text{tot}}$ where T_{tot} is defined in (8). However, when the TDM technique is adopted, more bits can be sent by other DLS pixels achieving a rate $R_{\text{TDM}} = N_{\text{TDM}}/T_{\text{tot}}$. In order to maximise the data rate and fully exploit the entire time frame as discussed in Section III-D, the number of required DLS pixels is $N_{\text{TDM}} = T_{\text{tot}}/T_{\text{sym}}$, then the maximum achievable data rate is $R = 1/T_{\text{sym}}$, where T_{sym} is determined in (7). Furthermore, when the polarization based modulation (4-PQAM) is employed allowing the communication of two bits simultaneously using two DLS pixels during each symbol duration, the data rate is multiplied by a factor of $L = \log_2(4) = 2$, and the maximum achievable data rate becomes $R = 2/T_{\text{sym}}$.

C. Throughput

To better understand the communication performance, we use the throughput defined as the rate of the successfully detected bits at the receiver. For one pair of DLS, the throughput $T_{\text{th}_{\text{DLS}}}$ is expressed as

$$T_{\text{th}_1} = 2R_{\text{DLS}} H_{\text{p}} \left(1 - P_{\text{error}_1}\right), \tag{55}$$

where H_{p} is the entropy and equal 1 for equiprobable symbols. As we employ TDM, the overall throughput of the system is

$$T_{\text{th}} = 2R_{\text{DLS}} \sum_{n=1}^{N_{\text{TDM}}} \left(1 - P_{\text{error}_{\text{n}}}\right), \tag{56}$$

where $P_{\text{error}_{\text{n}}}$ is the error probability corresponding to the n^{th} DLS pair.

VI. Simulation Results

In this simulation, we assume that the sunlight passes through a window embedded with our sunlight modulator to reach the receiver inside the room after travelling through the LOS link as displayed in Fig. 14. The Nematic LC-cells forming the DLS pixels of the modulator are based on the Electrically Controlled Birefringence (ECB) mode with parameters presented in Table I.

To obtain the DLS transmittance, we utilize the expressions in (19) and (20) which depend on the phase retardations $\delta_{i,\max} = \frac{2\pi d_i \Delta n_{i,\max}}{\lambda}$ and $\delta_{i,\min} = \frac{2\pi d_i \Delta n_{i,\min}}{\lambda}$, $i = 1, 2$ of each cell. Nonetheless, the LC characteristics including the the birefringence Δn_i and thickness d_i are usually not provided in the data sheets of commercially available LCDs. Hence, we adopt typical values of the parameters of Nematic LCDs, for instance the LC thickness ranges from 5 to $10\mu m$ and the typical birefringence range is $0.05 - 0.45$ [19].

To approximate the overall light transmission of the DLS, we optimize the transmittance of each cell to obtain the pulse waves in Fig. 7. Knowing that the extreme values of $\sin^2(\delta_1/2)$ and $\cos^2(\delta_2/2)$ are achieved when δ_1 and δ_2 are multiples of π, we estimate the corresponding birefringence values by setting $\delta_{1,\max} = \delta_{1,\min}$[3] to 3π, $\delta_{2,\min}$ to π and $\delta_{2,\max}$ to 2π, then averaging over the visible spectrum.

At the receiver side, we utilize identical APDs having parameters summarised in Table II, with the field of view $\psi_{\text{F}} = 75^\circ$ and the concentrator refractive index $n_c = 1.76$ [39]. We, also

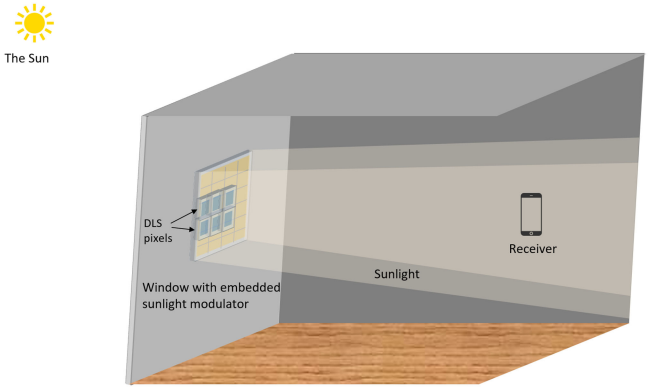

Fig. 14. Illustration of sunlight communication system in a room setup.

TABLE I
Parameters of the DLS

Parameter	Value
Opening time of Cell 1 ($\tau^{\text{open}}_{\text{NW}}$)	1.8 ms [36]
Closing time of Cell 1 ($\tau^{\text{close}}_{\text{NW}}$)	50 μs [36]
Opening time of Cell 2 ($\tau^{\text{open}}_{\text{NB}}$)	50 μs [36]
Closing time of Cell 2 ($\tau^{\text{close}}_{\text{NB}}$)	1.8 ms [36]
Thickness (d_1)	$6\mu m$
Birefringence ($\Delta n_{1,\max}$, $\Delta n_{2,\max}$,$\Delta n_{2,\min}$)	0.137, 0.092, 0.046
Transmittance of Polarizer 1 (α_1)	0.5
Transmittance of Polarizer 2 (α_2)	0.9 [37]
Transmittance of Polarizer 3 (α_3)	0.1, 0.9 [37]

TABLE II
Parameters of the APD [38]

Parameter	Value
Detection area (A_{APD})	19.6 mm^2
Gain (M)	50
Bandwidth (B)	8 MHz
Excess noise (F)	0.28
Temperature (T_{APD})	$298.15K$
Resistance (R_{T})	50 Ω
Dark current (I_{D})	3 nA

[3]The phase retardations are equal because cell 1 is in maximum transmission when sending "0" or "1" to eliminate flickering.

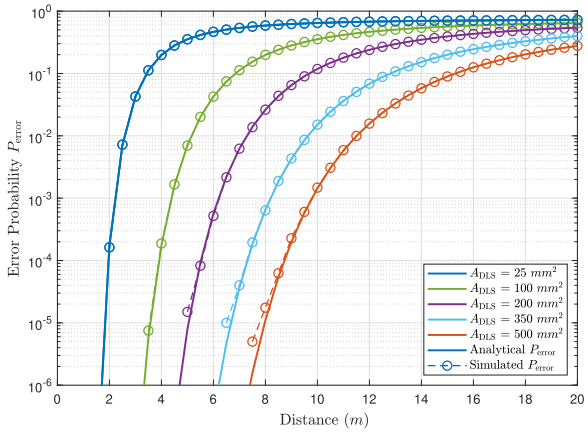

Fig. 15. Error probability versus link range for different DLS areas.

approximate the responsitivity of the APD using the curve provided in the data sheet [38] as follows

$$R_{APD}(\lambda) = 26.06 \exp\left(-\frac{(\lambda - 600)^2}{45000}\right),$$
$$300nm \leq \lambda \leq 1000nm. \quad (57)$$

Additionally, we assume that the channel gains are equal $h = h_1 = h_2$ and we set the time period T to 1 ns to maximise the achievable data rate, then the symbol duration $T_{\text{sym}} = 0.1\ ms$ and the total time frame $T_{\text{tot}} = 3.6\ ms$.

First of all, we consider the scenario where only a single DLS pair is operating during T_{tot} and having a perfect alignment with the pair of APDs. Fig. 15 presents the variation of the error probability versus the link range for different areas A_{DLS} of DLS pixel and demonstrates that the analytical and simulated P_{error} follow the same trend which validates the expressions derived analytically in the previous section. Besides, we observe that increasing the DLS area reduces the system's error probability which provides more reliable communication links over extended ranges. This is expected because larger DLS areas allow the passage of larger amounts of Sunlight such that it can travel farther in the indoor environment offering lower error probability for longer distances. Second, we investigate the performance of the modulator setup described in Section III-D having 6 DLS pixels in each group. The DLS pixels and APD positions are specified within the grid determined by the coordinate system defined in Section IV-C. The coordinates of the DLS pixels are $\{DLS_1, DLS_2, DLS_3, DLS_4, DLS_5, DLS_6\}$: $\{[(r_{\text{DLS}}, r_{\text{DLS}}), (3r_{\text{DLS}}, r_{\text{DLS}}), (5r_{\text{DLS}}, r_{\text{DLS}}), (r_{\text{DLS}}, 3 * r_{\text{DLS}}), (3r_{\text{DLS}}, 3r_{\text{DLS}}), (5r_{\text{DLS}}, 3r_{\text{DLS}})]\}$. We plot the error probability versus the link range for each DLS pair assuming that only one pair is transmitting during the total time frame. We also, place the APD pair at multiple positions to have different alignment conditions with each DLS pair. The plots are represented in Figs. 16–18 for different DLS areas.

In Fig. 16, the APD pair is placed at $(r_{\text{DLS}}, r_{\text{DLS}})$ having perfect alignment with the pair DLS_1. We first notice that P_{error} for DLS_1 is an increasing function of the distance regardless of the DLS area, and this is expected because of the perfect alignment. Then, we observe that for $A_{\text{DLS}} = 25\ mm^2$ [Fig. 16(a)], DLS_2 and DLS_4 follow the same increasing trend, while DLS_3, DLS_5 and DLS_6 have a similar decreasing/increasing behaviour. In fact, this is explained by the adjacency of the pixels. Since DLS_2 and DLS_4 are the nearest to DLS_1, the data would be received by the APD placed at $(r_{\text{DLS}}, r_{\text{DLS}})$ with minimum error for very short distances, then the error increases as the reduction in signal power for longer distances. Meanwhile, because of their remoteness from DLS_1, the information send by DLS_3, DLS_5 and DLS_6 is not properly reaching the APD for the same distances, resulting into high P_{error}, then as the link range extends, the error probability starts declining to reach its minimum when the footprints of DLS_3, DLS_5 and DLS_6 fully cover the APD area. Beyond that distance, P_{error} begins to follow the same trend as the other DLSs because their footprints cover the APD area similarly.

Moreover, as the DLS area enlarges ($A_{\text{DLS}} = 100\ mm^2$, 500 mm^2), the distance between the DLS_1 and other DLSs extends. Hence, knowing that the APD's area does not vary, the receiver should be located at farther ranges so that it can receive enough power from other DLSs. Consequently, the error probability follows the decline/rise trend for all other DLSs (adjacent or distant), except DLS_1, as shown in Fig. 16(b) and (c). We note, as well, that equivalent results can be found if the APD is considered to be perfectly aligned with any other DLS pair.

In addition, we inspect more general scenarios by changing the location of the APD. We initially, place it at the center of the group with coordinates $(3r_{\text{DLS}}, 2r_{\text{DLS}})$, then we choose an arbitrary position $(3.5r_{\text{DLS}}, 2.5r_{\text{DLS}})$. Figs. 17 and 18 display the corresponding P_{error} versus the link range. We observe similar trends, as in the case of perfect alignment, where the error probability depends on the proximity of the DLS to the APD as explained above. Nonetheless, Fig. 17 reveals that locating the APD at the center yields in indistinguishable curves and minimal P_{error} at each distance, for the different DLSs. This is due to the equidistant APD position from all DLSs. Thus, placing the APD at the center point is the optimal choice to minimise the error probability of the entire communication system.

Furthermore, we study the overall throughput performance of the system taking into account the TDM. Fig. 19 depicts the variations of the throughput T_{th} versus the communication range for various modulator setups. Assuming that the APD is placed at its center, each setup is identified by the number of DLS pairs N_{TDM} and the maximum achievable data rate R_{max}.

A common increasing/decreasing behaviour of the throughput can be observed in Fig. 19. In fact, as the receiver moves farther from the modulator, more DLS pairs contribute to the overall throughput allowing it to gradually rise. Then, the maximum throughput is achieved when the APD pair is located at a distance enabling it to receive data from all N_{TDM} DLS pairs. Subsequently, beyond a certain distance the throughput starts decreasing due to the low light intensity at longer communication ranges.

Another result, that can be deduced from Fig. 19, is that utilizing smaller number of DLS pairs, for instance $N_{\text{TDM}} = 6$, enables the system to attain its maximum achievable data rate $R_{\text{max}} = 3.33\ Kbps$. In contrast, employing larger number of

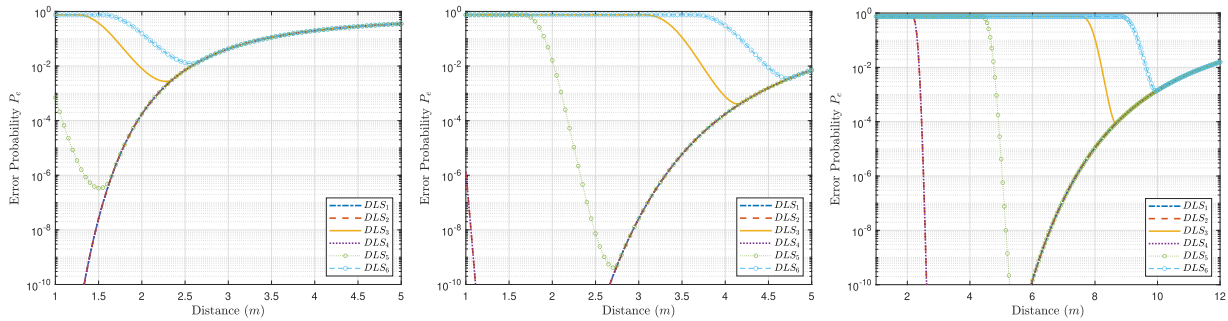

(a) A_{DLS} = 25 mm^2 (b) A_{DLS} = 100 mm^2 (c) A_{DLS} = 500 mm^2

Fig. 16. Error Probability versus link range for APD placed at $(r_{\mathrm{DLS}}, r_{\mathrm{DLS}})$.

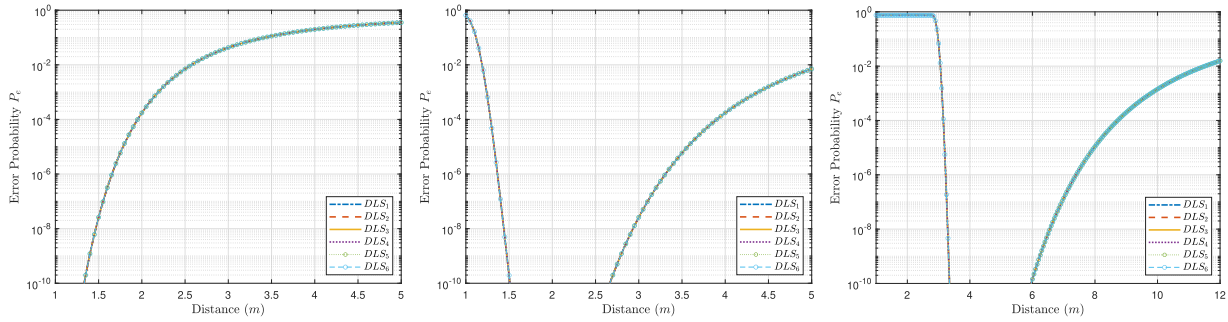

(a) A_{DLS} = 25 mm^2 (b) A_{DLS} = 100 mm^2 (c) A_{DLS} = 500 mm^2

Fig. 17. Error probability versus link range for APD placed at $(3r_{\mathrm{DLS}}, 2r_{\mathrm{DLS}})$.

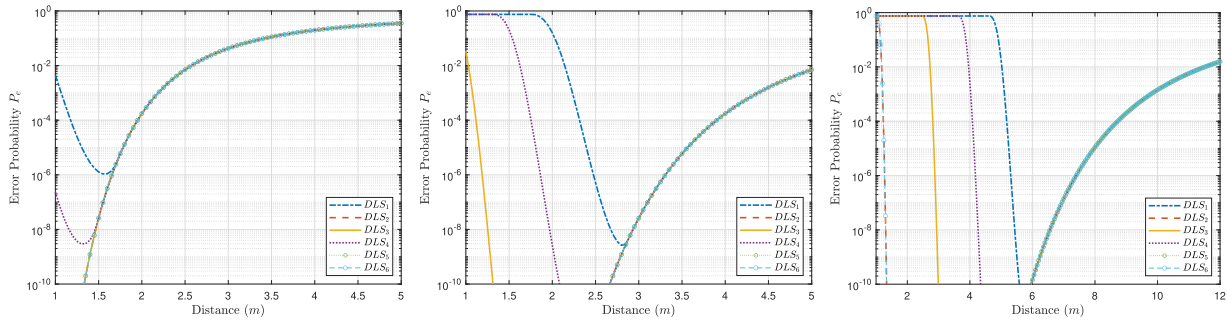

(a) A_{DLS} = 25 mm^2 (b) A_{DLS} = 100 mm^2 (c) A_{DLS} = 500 mm^2

Fig. 18. Error Probability versus link range for APD placed at $(3.5r_{\mathrm{DLS}}, 2.5r_{\mathrm{DLS}})$.

pairs ($N_{\mathrm{TDM}} = 25$ and $N_{\mathrm{TDM}} = 35$) limits the maximum overall throughput to values that are strictly lower than R_{max} (13.89 $Kbps$ and 19.44 $Kbps$). As a matter of fact, even though using greater N_{TDM} provides better throughput performance because more time frame can be exploited, the throughput can reach its maximum value, like in case of $N_{\mathrm{TDM}} = 6$, only if two conditions are verified; namely the receiver must to be located at a minimum distance from the modulator to allow the contribution of all DLS pairs and the received power from the DLSs at this distance should be high enough to establish a high data rate link. Lastly, we compare the performance of the proposed Sunlight system with the state-of-the-art (SoA). To conduct a fair comparison, we utilize approximately equal total modulator's areas as the SoA systems. The total area of our Sunlight modulator is defined as $A_{\mathrm{tot}} = 2N_{\mathrm{TDM}}A_{\mathrm{DLS}}$ supposing that the inter-spacing between DLS pixels is negligible.

To carry out our comparison, we choose two systems from the SoA in particular RetroTurbo [12] having a total modulator area $A_{\mathrm{tot}} = 66\ cm^2$ and PassiveVLC [13] with $A_{\mathrm{tot}} = 14\ cm^2$, their data rates are compared with the throughput curves in solid and dashed lines, respectively in Fig. 20. With setups having equivalent modulator areas as the SoA, our system outperforms the SoA and can operate over a range of 25 meters. When the number of pixels N_{TDM} required to fully exploit the total

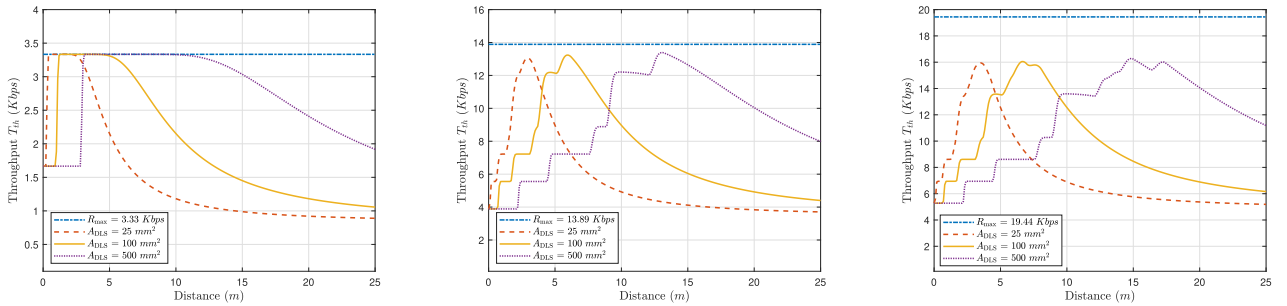

(a) $N_{\mathrm{TDM}} = 6$, APD at $(3r_{\mathrm{DLS}}, 2r_{\mathrm{DLS}})$ (b) $N_{\mathrm{TDM}} = 25$, APD at $(5r_{\mathrm{DLS}}, 5r_{\mathrm{DLS}})$ (c) $N_{\mathrm{TDM}} = 35$, APD at $(7r_{\mathrm{DLS}}, 5r_{\mathrm{DLS}})$

Fig. 19. Overall throughput versus link range for different modulator setups.

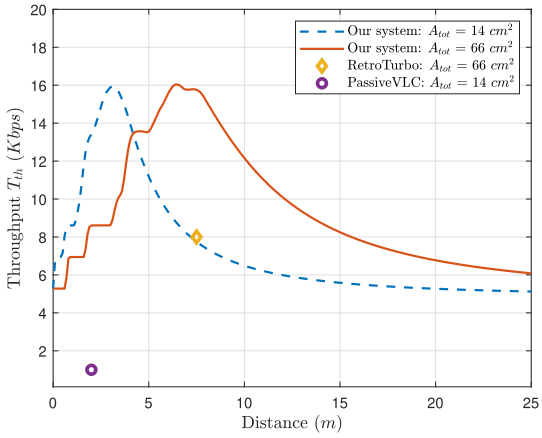

Fig. 20. Comparison with the state-of-the-art.

time duration is used, our system achieves around 16 $Kbps$ of throughput at a link range of 7.5 m, while RetroTurbo has a data rate of 8 $Kbps$. As for PassiveVLC, it presents 1 $Kbps$ as data rate for a distance of 2 m, while the maximum throughput of the proposed system is about 16 $Kbps$ for the same total area.

VII. Energy Consumption Analysis

As shown in Fig. 7, a voltage, is applied to each Liquid Crystal cell to allow the proper design of the pulse wave of the transmitted bit. In fact, for Cell 1 which is working in NW manner, the presence of an electrical field is required during the the closing time $\tau_{\mathrm{NB}}^{\mathrm{close}}$ of Cell 2 when either bit "0" or "1" is sent. Also, for Cell 2 with NB operation, a voltage is applied during the time interval $T + \tau_{\mathrm{NB}}^{\mathrm{open}}$ when bit "1" is transmitted.

The electrical energy is defined as the product of the average electrical power and the time interval. So, the energy required for data transmission per bit, using one DLS pixel, is given by

$$\begin{aligned} E_1 &= P_{\mathrm{RMS}}(V_1, I_1) \times \tau_{\mathrm{NB}}^{\mathrm{close}} + P_{\mathrm{RMS}}(V_2, I_1) \times \left(T + \tau_{\mathrm{NB}}^{\mathrm{open}}\right), \\ E_0 &= P_{\mathrm{RMS}}(V_1, I_1) \times \tau_{NB}^{\mathrm{close}}, \end{aligned} \tag{58}$$

where V_1, V_2 and I_1 are the RMS voltage and current values of each LC cell. Thus, the average energy required for the operation

TABLE III
Approximation of the Sunlight Modulator RMS Power Consumption [36]

RMS Power Consumption	
Average power for one LC cell P_{RMS}	$12mW$
Voltage value for one LC cell V_1	$12.73V$
Current value for one LC cell I_1	$0.019A$
Average power for one DLS pixel P_{DLS}	$11.84mW$
Average total power P_{R}	$0.83W$

of one DLS pixel is

$$\begin{aligned} E &= p_1 E_1 + p_0 E_0 \qquad (p_1 = p_0 = 0.5) \\ &= P_{\mathrm{DLS}} \times \left(\tau_{\mathrm{NB}}^{\mathrm{close}} + T + \tau_{NB}^{\mathrm{open}}\right). \end{aligned} \tag{59}$$

Then, the average power is $P_{\mathrm{DLS}} = E/\left(\tau_{\mathrm{NB}}^{\mathrm{close}} + T + \tau_{\mathrm{NB}}^{\mathrm{open}}\right)$, and taking into account the total number of DLS pixels N_{pixel} required to achieve the maximum data rate R, the total electrical power becomes $P_{\mathrm{R}} = N_{\mathrm{pixel}} P_{\mathrm{DLS}}$. So, to fulfill the energy needs of the modulator, we use a solar cell to harvest the Sunlight energy. If we consider the modulator as a parallel circuit where the DLS pixels are the components placed in parallel and we determine the number of DLSs that needs an electrical power during the same time frame to achieve the proper operation of the design, then the required voltage and current are defined as $V_{\mathrm{OC}} = \max\{V_1, V_2\}$ and $I_{\mathrm{SC}} = \lceil N_{\mathrm{TDM}}/2 \rceil I_1$, where $\lceil x \rceil$ is the ceiling function. Hence, the solar panel should provide a maximum electrical power P_{R}, with open circuit voltage V_{OC} and short circuit current I_{SC}.

In order to properly function, the LC cells require an AC voltage with a peak value in the range of 2-30 V in general. Knowing that the switching times of the DLS are highly effected by the applied voltage, and thus directly related to the DLS's energy needs, we base this energy consumption analysis on the available data in the data sheet [36]. Table III lists the voltage V_1, current I_1 and average power P_{RMS} RMS values needed for the operation of one LC cell. Also, we approximate the average power needed by one DLS pixel $P_{\mathrm{DLS}} \approx 10mW$, and the total power $P_{\mathrm{R}} \approx 1W$ needed to reach the maximum data rate R. Therefore, such low power requirements can be fulfilled by the solar panel whose approximated specifications are summarized in Table IV.

TABLE IV
APPROXIMATED SPECIFICATIONS OF THE SOLAR PANEL

Solar cell specifications	
Maximum power P_{R}	1 W
Open Circuit voltage V_{OC}	13 V
Short Circuit current I_{SC}	0.4 A

VIII. CONCLUSION

In this work, we proposed and analysed the performances of an LCD-based passive Sunlight communication system. We designed a novel Dual-cell Liquid Crystal Shutter (DLS) by stacking two LC cells operating in opposite manners. The DLS offered fast and equal opening and closing times. Additionally, with the proper design of the pulse waves, the DLS mechanism addressed the issues of the flicker effect and the inter-symbol interference. Then, we developed a Sunlight modulator that efficiently utilizes of time and polarization dimensions to boost the data rate and we provided the theoretical analysis of the proposed system with simulation results. For future work, we are interested in the implementation of the Sunlight communication system and experimental performance evaluation will be conducted.

REFERENCES

[1] A. M. Abdelhady, O. Amin, M.-S. Alouini, and B. Shihada, "Revolutionizing optical wireless communications via smart optics," *IEEE Open J. Commun. Soc.*, vol. 3, pp. 654–669, 2022.

[2] Q. Wang and M. Zuniga, "Passive visible light networks: Taxonomy and opportunities," in *Proc. Workshop Light Up IoT*, 2020, pp. 42–47.

[3] S. D. Rezaei, S. Shannigrahi, and S. Ramakrishna, "A review of conventional, advanced, and smart glazing technologies and materials for improving indoor environment," *Sol. Energy Mater. Sol. Cells*, vol. 159, pp. 26–51, Jan. 2017.

[4] B. Lamontagne, N. R. Fong, I.-H. Song, P. Ma, P. J. Barrios, and D. Poitras, "Review of microshutters for switchable glass," *J. Micro/Nanolithography, MEMS MOEMS*, vol. 18, no. 4, Oct. 2019, Art. no. 040901.

[5] R. Bloom, M. Z. Zamalloa, and C. Pai, "LuxLink: Creating a wireless link from ambient light," in *Proc. 17th Conf. Embedded Networked Sensor Syst.*, 2019, pp. 166–178.

[6] H. H. Hillmer, M. S. Q. Iskhandar, M. K. Hasan, S. Akhundzada, B. Al-Qargholi, and A. Tatzel, "MOEMS micromirror arrays in smart windows for daylight steering," *J. Opt. Microsystems*, vol. 1, no. 1, Jan. 2021, Art. no. 014502.

[7] D. Stekovic and M. E. Itkis, "Phenalenyl based neutral radical as a novel electrochromic material modulating visible to short-wave infrared light," *RSC Adv.*, vol. 8, no. 73, pp. 42068–42072, Dec. 2018.

[8] G. Yang et al., "Advances in nanomaterials for electrochromic devices," *Chem. Soc. Rev.*, vol. 49, no. 23, pp. 8687–8720, Oct. 2020.

[9] B. Lamontagne, P. Barrios, C. Py, and S. Nikumb, "The next generation of switchable glass: The micro-blinds," in *Proc. Conf. Glass Perform. Days*, 2009, pp. 50–53.

[10] K.-H. Lee, J. Chang, and J.-B. Yoon, "High performance microshutter device with space-division modulation," *J. Micromechanics Microengineering*, vol. 20, no. 7, Jun. 2010, Art. no. 075030.

[11] L.-T. D. AB, "FOS (fast optical shutter) series model overview," 2016. [Online]. Available: https://www.lc-tec.se/wp-content/uploads/2019/05/FOS-series-model-overview-1611.pdf

[12] Y. Wu, P. Wang, K. Xu, L. Feng, and C. Xu, "Turboboosting visible light backscatter communication," in *Proc. Annu. Conf. ACM Special Int. Group Data Commun. Appl. Technol., Architectures Protoc. Comput. Commun.*, 2020, pp. 186–197.

[13] X. Xu et al., "PassiveVLC: Enabling practical visible light backscatter communication for battery-free IoT applications," in *Proc. 23th Annu. Int. Conf. Mobile Comput. Netw.*, 2017, pp. 180–192.

[14] J. Li, A. Liu, G. Shen, L. Li, C. Sun, and F. Zhao, "*Retro-VLC*: Enabling battery-free duplex visible light communication for mobile and IoT applications," in *Proc. ACM 16th Int. Workshop Mobile Comput. Syst. Appl.*, 2015, pp. 21–26.

[15] P. Wang et al., "Renovating road signs for infrastructure-to-vehicle networking: A visible light backscatter communication and networking approach," in *Proc. 26th Annu. Int. Conf. Mobile Comput. Netw.*, 2020, pp. 1–13.

[16] S. Shao, A. Khreishah, and H. Elgala, "Pixelated VLC-backscattering for self-charging indoor IoT devices," *IEEE Photon. Technol. Lett.*, vol. 29, no. 2, pp. 177–180, Jan. 2017.

[17] S. K. Ghiasi, M. A. Z. Zamalloa, and K. Langendoen, "A principled design for passive light communication," in *Proc. 27th Annu. Int. Conf. Mobile Comput. Netw.*, 2021, pp. 121–133.

[18] Z. Yang, Z. Wang, J. Zhang, C. Huang, and Q. Zhang, "Wearables can afford: Light-weight indoor positioning with visible light," in *Proc. 13th Annu. Int. Conf. Mobile Syst. Appl. Serv.*, 2015, pp. 317–330.

[19] P. Yeh and C. Gu, *Optics of Liquid Crystal Displays*. Hoboken, NJ, USA: Wiley, 1999.

[20] E. Collett, *Field Guide to Polarization*. Bellingham, WA, USA: SPIE, 2005.

[21] S. Kelly and M. O'Neill, "Chapter 1 - Liquid crystals for electro-optic applications," in *Handbook of Advanced Electronic and Photonic Materials and Devices*, New York, NY, USA: Academic, 2001, pp. 1–66.

[22] BOLDER VISION OPTIK, INC., "Nematic liquid crystal devices," 2021. [Online]. Available: http://boldervision.com/liquid-crystals/

[23] P. J. Bos and K. R. Koehler/Beran, "The pi-Cell: A fast liquid-crystal optical-switching device," *Mol. Cryst. Liquid Cryst.*, vol. 113, no. 1, pp. 329–339, Dec. 1984.

[24] D.-K. Yang and S.-T. Wu, *Fundamentals of Liquid Crystal Devices*. Hoboken, NJ, USA: Wiley, 2014.

[25] C. H. Gooch and H. A. Tarry, "The optical properties of twisted nematic liquid crystal structures with twist angles ≤ 90 degrees," *J. Phys. D: Appl. Phys.*, vol. 8, no. 13, pp. 1575–1584, Sep. 1975.

[26] C. H. Gooch and H. A. Tarry, "Optical characteristics of twisted nematic liquid-crystal films," *Electron. Lett.*, vol. 10, no. 1, pp. 2–4, Jan. 1974.

[27] R. Soref and M. Rafuse, "Electrically controlled birefringence of thin nematic films," *J. Appl. Phys.*, vol. 43, no. 5, pp. 2029–2037, May 1972.

[28] L. M. Blinov and V. G. Chigrinov, *Electrooptic Effects in Liquid Crystal Materials*. Berlin, Germany: Springer Science & Business Media, 1996.

[29] J. E. Yellowhair, *Field Guide to Solar Optics*. Bellingham, WA, USA: SPIE, 2020.

[30] N. R. E. Laboratory, "Reference air mass 1.5 spectra," 2021. [Online]. Available: https://www.nrel.gov/grid/solar-resource/spectra-am1.5.html

[31] A. A. Mills and R. Clift, "Reflections of the 'burning mirrors of archimedes'. With a consideration of the geometry and intensity of sunlight reflected from plane mirrors," *Eur. J. Phys.*, vol. 13, no. 6, pp. 268–279, Nov. 1992.

[32] J. E. Greivenkamp, *Field Guide to Geometrical Optics*. Bellingham, WA, USA: SPIE, 2004.

[33] Z. Ghassemlooy, W. Popoola, and S. Rajbhandari, *Optical Wireless Communications: System and Channel Modelling With Matlab*. Boca Raton, FL, USA: CRC Press, 2019.

[34] G. Keiser, *Optical Communications Essentials*. New York, NY, USA: McGraw-Hill Education, 2003.

[35] A. Trichili, M. A. Cox, B. S. Ooi, and M.-S. Alouini, "Roadmap to free space optics," *J. Opt. Soc. Amer. B*, vol. 37, no. 11, pp. A184–A201, Nov. 2020.

[36] L.-T. D. AB, "X-fos(g2)/x-fos(g2)-ar," 2016. [Online]. Available: https://www.lc-tec.se/fast-optical-shutters/

[37] BOLDER VISION OPTIK, INC., "Bvo 244 polarizer," 2020. [Online]. Available: http://boldervision.com/linear-polarizers/bvo-244-polarizer/

[38] H. Photonics, *Si APD*, "Datasheet, Avalanche photodiodes (APDs)," 2013. [Online]. Available: https://www.hamamatsu.com/eu/en/product/optical-sensors/apd/si-apd.html

[39] A. M. Abdelhady, O. Amin, A. Chaaban, B. Shihada, and M.-S. Alouini, "Spectral-efficiency—illumination pareto front for energy harvesting enabled VLC systems," *IEEE Trans. Commun.*, vol. 67, no. 12, pp. 8557–8572, Dec. 2019.